NTNU

Norwegian University of
Science and Technology

Development of Transmit and Receive Coils for 1H MRI/MRS on a 7T MR Scanner

Alexander Craig-Craven

Master of Science in Engineering Cybernetics

Submission date: June 2010

Supervisor: Tor Engebret Onshus, ITK

Co-supervisor: Øystein Risa, Den Medisinske Fakultet, Institutt for Sirkulasjon og Bildediagnostike

Asta Håberg, Den Medisinske Fakultet, Institutt for Sirkulasjon og Bildediagnostike

Norwegian University of Science and Technology
Department of Engineering Cybernetics

Problem Description

Introduction:

High quality pictures with good resolution are of crucial importance in magnetic resonance imaging (MRI). Due to the relative low intrinsic sensitivity of the MR-technology there are high demands on the specific hardware equipment. The technical design of the radio frequency (RF) coils is one of the components that are of crucial importance to get as high signal to niose ratio as possible in the images.

The medical faculty at NTNU have a high field (7T) MR-scanner for animals. Main research activity are focusing on brain, heart and cancer diseases.

The aim of the study:

The project involve building two different surface transmit/receive coils.
One for 1H MRI and MRS and one for 31P MRS.

We will first build and test the 1H coil and compare the image quality on phantoms to other coils in house. After building the coil and the comparison testing is finished the 1H coil will be used to study tumours in rats. The shape of the coil is of crucial importance for optimal testing of these tumours.

Second we will build a 31P surface coil. The quality of the coil will be tested on phantoms.
The main application for this coil will be 31P MRS on rat heart and brain.

Methods:

It is important that the student is capable of understanding simple electronic circuits and understand how a coil will behave in a strong magnetic field. The student must know how to use a copper bit and also how to use electronic equipment such as an oscilloscope and voltmeter. Basic knowledge of MR theory is mandatory. As mentioned above will the coils be tested on our 7T animal scanner and practical experience of running an MR-scanner is an advantage. However a full training of the student on running MR experiments will be given.

Assignment given: 14. January 2010
Supervisor: Tor Engebret Onshus, ITK

Development of transmit and receive coils for Proton MRI at a 7T MR-scanner for animals.

Alex Craven

June 2010

Norwegian University of Science and Technology, Trondheim
Under the supervision of Øystein Risa (Institutt for Sirkulasjon og Bildediagnostikk), Tor Onshus (Institutt for Teknisk Kybernetikk) and Asta Håberg (Institutt for Nevromedisin)

Abstract

High quality images with strong contrast, good resolution and geometrical consistency are of crucial importance in magnetic resonance imaging, where the relatively low intrinsic sensitivity of magnetic resonance methods places high demands on the imaging hardware. One of many key components in the imaging system is the radiofrequency coil, responsible for transmitting excitation signals and/or listening for response from the object. In this project a number of such coils are developed for specific applications (namely proton (^{1}H) imaging of rat and fish brains), then evaluated empirically and against phantoms in simulated imaging situations. Evaluation of the produced coils shows promising initial results, with various opportunities for further refinement into a device suitable for regular use.

Contents

Preface x

I Introduction 1

1 Overview 2
1.1 Motivation . . . 2
1.2 Structure . . . 2

2 Theoretical Background 4
2.1 Overview . . . 4
2.2 Introduction to Magnetic Resonance Imaging . . . 4
2.2.1 Nuclear Magnetic Resonance . . . 4
2.2.1.1 Alternative Nuclei . . . 5
2.2.2 Motion of Magnetic Moments in an Applied Field . . . 6
2.2.3 Relaxation Processes and The Bloch Equations . . . 6
2.2.3.1 Longitudinal Relaxation (T_1) . . . 7
2.2.3.2 Transverse Relaxation (T_2) . . . 7
2.2.4 High field Strengths . . . 7
2.2.5 Spatially Localised Nuclear Magnetic Resonance for Imaging . . . 8
2.3 Pulse Sequences for Imaging . . . 8
2.3.1 The Spin-Echo (SE) Imaging Sequence . . . 9
2.3.2 Contrast and Weighting . . . 10
2.3.2.1 T_1 Weighting . . . 10
2.3.2.2 T_2 Weighting . . . 10
2.3.2.3 Spin Density Weighting . . . 10
2.3.3 The Gradient Echo (GE) Sequence . . . 10
2.4 RF Coil Design for Magnetic Resonance Imaging . . . 11
2.4.1 Electromagnetic Response and the Biot Savart Law . . . 11
2.4.2 Tuning and Matching . . . 12
2.4.3 Quality (Q) Factor . . . 12
2.4.4 High-field Considerations . . . 12
2.4.5 Additional Features . . . 13
2.5 Physical Design and Material Selection for MR applications . . . 14
2.6 Aspects of Image Quality . . . 14
2.6.1 Sensitivity and Signal to Noise Ratio . . . 14
2.6.2 Specific Absorption Rate (SAR) . . . 16

2.6.3 Imaging Artifacts 16

II Materials, Methodology, Implementation 17

3 Tools and Materials 18
3.1 Target Hardware 18
3.2 Design Tools 18
3.3 Fabrication 19
3.4 Characterization and Tuning 19
3.5 Evaluation 20

4 Methodology 21
4.1 Overview 21
4.2 Design Process 21
4.2.1 Electromagnetic Design and $\mathbf{B}_1$ Field 21
4.2.2 Electronic Design 22
4.2.2.1 Q estimation 22
4.3 Prototyping 22
4.3.1 Tuning and Matching 23
4.4 Evaluation 23

5 Small Loop ^{1}H Surface Coils 24
5.1 Introduction 24
5.2 Methodology 24
5.2.1 Basic Geometry 24
5.2.2 Circuit Model 24
5.2.2.1 Multi-turn wire geometry 26
5.2.2.2 Washer geometry 27
5.2.2.3 Single-turn geometry 27
5.2.2.4 Simplifications in the Circuit Model 27
5.2.3 Tuning and Matching 28
5.2.4 Coil Design 29
5.2.4.1 Wire Gauge 29
5.2.4.2 Conductor length and capacitive splits 31
5.2.4.3 Electromagnetic Simulation 31
5.2.5 Physical implementation 32
5.2.5.1 Small loop (version zero) 32
5.2.5.2 Small loop (version one) 32
5.2.5.3 Small loop (version two) 33
5.2.6 Preliminary Tuning and Matching 33

6 Helmholtz Coil for In Vivo Imaging of a Fish Brain 34
6.1 Introduction 34
6.2 Methodology 35
6.2.1 Basic Geometry 35
6.2.2 Circuit Model 36
6.2.3 Tuning and Matching 36
6.2.4 Physical Implementation 37

III Evaluation **38**

7 Procedures **39**
7.1 Q-factor . . . 39
7.2 Signal to Noise Ratio (SNR) Estimation . . . 39
7.3 Usable Area/$\mathbf{B}_1$ Homogeneity . . . 41
7.4 Image Intensity Uniformity . . . 41
7.5 Artifacts . . . 42
7.6 Evaluation Configuration . . . 42
7.6.1 Test Subjects . . . 42
7.6.2 Test objects . . . 43
7.6.3 Test Hardware . . . 44
7.7 Practical procedure . . . 45
7.7.1 Preparation . . . 45
7.7.2 Measurements in the magnet . . . 45
7.7.3 Measurements on the Network Analyzer . . . 46
7.7.4 Post-processing and Analysis of the Acquired Images . . . 47
7.7.4.1 Software Requirements . . . 47
7.7.4.2 Analysis procedure . . . 47

8 Results **48**
8.1 Coil Response and Quality Factor . . . 48
8.2 Signal Quality as Measured on the Scanner . . . 48
8.3 Imaging Artifacts . . . 51
8.4 Image Acquisition . . . 52

9 Discussion **53**
9.1 Coil Response and Quality Factor . . . 53
9.2 Tuning and Matching . . . 53
9.3 Image Quality . . . 53
9.4 Imaging Area . . . 54
9.5 Imaging Artifacts . . . 54
9.6 Practical Considerations . . . 54
9.6.1 Tuning and Matching controls . . . 54
9.6.2 Housing . . . 55
9.6.3 Affects of Loading and Cable Orientation . . . 55

10 Further work **56**

11 Conclusions **57**

IV Appendices **58**

A Raw Results **59**
A.1 Overview . . . 59
A.2 Small loop (version one) . . . 61
A.3 Small loop (version two) . . . 62
A.4 Helmholtz coil . . . 63
A.5 Bruker 300-75 . . . 64

B Components **65**

Bibliography **67**

List of Tables

2.1 Mass Susceptibility of various materials 14
2.2 Maximising the received Signal to Noise ratio – tradeoffs 15

8.1 Coil response and quality factor 48
8.2 Summary of Image Quality Measurements 49

List of Figures

2.1 The basic Spin-Echo imaging sequence 9
2.2 The Gradient Echo imaging sequence 11

3.1 Fabrication facilities 19

4.1 Tuning and matching a coil 23

5.1 Basic circuit model for a single resonant RF coil 25
5.2 Skin depth 25
5.3 Tune-and-match circuit 29
5.4 Coil simulation in Spice 30
5.5 Full-wave simulation of the small loop coil 31
5.6 Preliminary implementation of the ^{1}Hcoil 32
5.7 First practical implementation of the ^{1}H coil 32
5.8 PCB layout for Small loop (version one) 33
5.9 Second practical implementation of the ^{1}H coil 33

6.1 Field strength along the axis of a helmholtz coil 35
6.2 Placement of the Helmholtz coil for fish brain imaging 35
6.3 Circuit model for the Helmholtz Coil 36
6.4 Implementation of the Helmholtz coil 37

7.1 Images used in the NEMA method for SNR estimation 41
7.2 Surface coils for evaluation 43
7.3 Phantoms used for testing 43
7.4 Bruker 7T Small Animal Scanner 44
7.5 Network Analyzer for out-of-magnet measurements 45

8.1 Artifacts observed when imaging with Small loop (version two) 51
8.2 Imaging Performance 52

Nomenclature

$\mathbf{B}_0$	Static magnetic field (typically from the main magnet of an MR machine)
$\mathbf{B}_1$	Excitation magnetic field from the RF coil
γ	Gyromagnetic ratio
C	Capacitance
δ	Skin depth
e	Electron charge
EM	Electromagnetic
ESR	Effective Series Resistance of a capacitor
f_0	Larmor frequency
FOV	Field of View of a scan
GE	Gradient Echo imaging pulse sequence (section 2.3.3)
g	Guage (diameter) of a wire conductor
H	Material-dependant description of magnetic field strength
^{1}H	Notation for proton imaging
$\mathbf{I}$	Electronic current
ITK	Institutt for Teknisk Kybernetikk (at NTNU)
j	Complex number notation, $\sqrt{-1}$
λ	Wavelength
L	Inductance
M	Net magnetization
m	Magnetic dipole moment
μ	Permeability of a material (μ_0 for free space)
m	Proton mass

MRI	Magnetic Resonance Imaging
MR	Magnetic Resonance
MRS	Magnetic Resonance Spectroscopy
NTNU	Norwegian University of Science and Technology
PCB	Printed Circuit Board
Q	Quality factor
ρ	Resistivity of a material (ρ_0 for free space)
RFI	Radio Frequency Interference
RF	Radio Frequency, with reference to excitation pulses and coils for generation thereof
ROI	Region Of Interest within an image
RoHS	Restriction of Hazardous Substances directive
R	Resistance
SAR	Specific Absorption Rate
SE	Spin Echo imaging pulse sequence (section 2.3.1)
SNR	Signal to Noise Ratio
S	Various measures of signal strength
$\mathbf{T}$	Torque vector
T	Tesla, standard unit for magnetic field strength
T_1	Longitudinal relaxation time
T_2	Transverse relaxation time
T_2^*	Effective transverse relaxation time
TE	Echo time for a pulse sequence
TR	Repetition time for a pulse sequence
v	Voltage
X	Reactance
ω_0	Larmor frequency, angular
z	Axis typically defined by the direction of the main $\mathbf{B}_0$ field in imaging hardware
Z	Impedance, $\mathrm{Z} = \mathrm{R} + j\mathrm{X}$

Preface

This document describes work undertaken towards a master thesis, constituent of a Master of Science program at the Norwegian University of Science and Technology (NTNU, Trondheim). The underlying work was performed at the Department of Circulation and Medical Imaging during spring 2010, under the guidance and supervision of Øystein Risa, Tor Onshus and Asta Håberg. Thanks must go to these supervisors for their support throughout the project, to John Olav Horrigmo (Institutt for Teknisk Kybernetikk) and Terje Mathiesen (Institutt for Elektronikk og Telekommunikasjon) for providing equipment and support necessary for the construction and testing of the devices, and to Veronika for her ongoing support and feedback.

Part I

Introduction

Chapter 1

Overview

1.1 Motivation

High quality images with good resolution, contrast and geometrical consistency are of crucial importance in magnetic resonance imaging (MRI). The relatively low intrinsic sensitivity of MR methods places high demands on imaging hardware. The design of radiofrequency (RF) coils is one of many aspects critical to obtaining suitable signal strength and optimal signal to noise ratio in the acquired images. Surface coils, concentrating the RF power in a particular area of interest, provide various potential advantages in these areas over broader volume coils.

In this project, design, construction and evaluation of transmit/receive surface coils for use in a high field MR-scanner for animals was to be performed. This scanner is situated in the medical faculty at NTNU, with research activity focusing on brain, heart and cancer diseases. Coils will be developed for proton (^{1}H) MRI of rats, and for imaging of the brain of a live fish.

Initially, a basic ^{1}H coil was to be built and tested on phantoms, with image quality compared with other coils available in-house. After construction and comparison testing is complete, the ^{1}H coil may be used to study tumours in rats. Additionally, a specialised design for in-vivo imaging of a fish brain was to be developed.

Numerous surface coil implementations are commercially available, offering very good performance for general-purpose imaging. Nonetheless, many imaging applications benefit from the development of a specialized coil adapted to the unique geometry and properties of the object of interest. Hence, an additional function of this project is to assess the feasibility and effectiveness of developing RF coils in-house, to evaluate their performance and viability relative to commercially available products and to provide a basic framework for further developments in this area.

1.2 Structure

This document is divided into three parts; in the first (current) part, the fundamental nature of the project and the basic theory underlying the technologies involved are introduced. Design challenges and parameters are identified, and

objectives with respect to these are nominated. In the second part, the approach to the design is presented and executed in the context of material from the earlier part. In the final part, the resulting designs are evaluated in simulated imaging environments, and assessed visually and analytically with suitable standard metrics.

Chapter 2

Theoretical Background

2.1 Overview

In this section, a basic introduction to magnetic resonance imaging, the role of the surface coil and design considerations for this are discussed. Fundamental physical and electromagnetic principles underpinning the concepts described here are briefly mentioned, with additional references presented for more detailed explanation.

In order to appreciate the design criteria and specific challenges associated with coil development for high-field MRI, it is first necessary to examine the basic principles both of magnetic resonance imaging and of electromagnetic coil design and characterisation; these are dealt with separately in the following sections.

2.2 Introduction to Magnetic Resonance Imaging

Nuclear Magnetic Resonance Imaging (MRI) techniques involve the manipulation and observation of nuclear magnetic moments intrinsic to matter for generation of an image describing the structural properties of that matter.

In this section, the physics underlying magnetic resonance imaging techniques is investigated, with explanation of how this may be utilised to obtain spatially-resolved images characterising material parameters. A rigorous reference on the subject is provided in [Haacke et al., 1999], whilst a more accessible, intuitive discussion may be found in [Westbrook et al., 2005].

2.2.1 Nuclear Magnetic Resonance

Nuclear Magnetic Resonance operates most fundamentally by manipulating spin states of individual nuclei in a material. Whilst an in-depth quantum mechanical description may be formulated dealing with the statistical distribution of spin states in the material, for the purposes of this report it is sufficient to begin with a classical description describing the *net* nuclear magnetic moment of the material, as presented in [Webb, 1988] and [Kuperman and Kuperman, 2000].

In the classical description, an isolated proton with a charge $+e$ and angular momentum $\mathbf{I}$ is initially considered. As described by Maxwell's equations (pre-

sented in [Maxwell, 1865] and summarised in [Sadiku, 2001] amongst countless others) an electronic charge circulating in a conducting loop produces a magnetic field normal to the plane of current rotation. Considering the proton charge to be distributed and rotating along a central axis as a result of the angular momentum, a magnetic dipole moment $\mathbf{m}_p$ antiparallel to the angular momentum vector (and hence, normal to the plane of charge circulation) results, ie, $\mathbf{m}_p = \gamma\mathbf{I}$

γ describes the gyromagnetic ratio, which for the simplified classic model is given by:

$$\gamma = \frac{e}{2m} \tag{2.2.1}$$

where m is the proton mass.

An external magnetic flux density $\mathbf{B}_0$ will exert a torque $\mathbf{T}$ on a magnetic dipole moment, causing the angular momentum to change at a rate equal to the torque, i.e.

$$\mathbf{T} = \mathbf{m}_p \times \mathbf{B}_0 \tag{2.2.2}$$

$$= \frac{d\mathbf{I}}{dt} \tag{2.2.3}$$

$$\text{and hence, } \frac{d\mathbf{m}_p}{dt} = \gamma\mathbf{m}_p \times \mathbf{B}_0 \tag{2.2.4}$$

The result in equation 2.2.4 is the *Larmor equation*, which describes the precession of the magnetic dipole moment $\mathbf{m}_p$ about $\mathbf{B}_0$ with angular velocity

$$\omega_0 = -\gamma\mathbf{B}_0$$

Substituting equation 2.2.1, the Larmor frequency for the single proton described here is therefore given by

$$f_0 = \frac{\gamma}{2\pi} \tag{2.2.5}$$

$$= 42.58\text{MHz/T} \tag{2.2.6}$$

$$= 298.06\text{MHz (for protons at 7T)} \tag{2.2.7}$$

In MRI applications, the static, homogeneous $\mathbf{B}_0$ field described here is presented by the main field magnet. The magnetic dipole moment $\mathbf{m}_p$ may be dissected into a component parallel to $\mathbf{B}_0$, denoted m_{pz} where $\mathbf{B}_0$ defines the z direction, and a component m_{pxy} in the plane perpendicular to $\mathbf{B}_0$. For convenience of analysis, it can be helpful to examine the process in a coordinate system which rotates about the z axis at a frequency ω_0, in which dipoles rotating at frequency ω_0 appear stationary and any observable rotation about the z axis corresponds to a deviation from ω_0 arising from variations in the Larmor frequency – typically due to differences in field strength.

2.2.1.1 Alternative Nuclei

The simplest nucleus to be considered is the single proton, ^{1}H. Notwithstanding, similar principles may be applied to imaging or measuring various other

more complicated nuclei, such as $^{13}\mathrm{C}$, $^{31}\mathrm{P}$, $^{19}\mathrm{F}$ and $^{23}\mathrm{Na}$. Although the quantum mechanical behaviour is more complicated, the behaviour of the net magnetic moment in these cases is analogous; only the change in Larmor frequency (generally somewhat lower than for $^{1}\mathrm{H}$) needs to be considered. Whilst $^{1}\mathrm{H}$ imaging usually gives the strongest signal (being the most sensitive nuclei and abundant in biological tissue which contains a large proportion of water), other isotopes may provide more useful measurements for particular tissue types in certain applications, for either imaging or spectroscopy (MRS) purposes.

2.2.2 Motion of Magnetic Moments in an Applied Field

The motion of a magnetic moment in a static field is described by equation 2.2.4, which has a solution of the form:

$$\mathrm{m}_x(t) = \mathrm{m}_x(0)\cos\omega_0 t + \mathrm{m}_y(0)\sin\omega_0 t \tag{2.2.8}$$
$$\mathrm{m}_y(t) = \mathrm{m}_y(0)\cos\omega_0 t - \mathrm{m}_x(0)\sin\omega_0 t \tag{2.2.9}$$
$$\mathrm{m}_z(t) = \mathrm{m}_z(0) \tag{2.2.10}$$

In the presence of an applied field $\mathbf{B}_1$, equation 2.2.4 becomes:

$$\frac{d\mathbf{m}_p}{dt} = \gamma\mathbf{m}_p \times (\mathbf{B}_0 + \mathbf{B}_1) \tag{2.2.11}$$

In MRI applications, the additional $\mathbf{B}_1$ field is typically an RF field 'rotating' at a frequency of ω and orientated normal to the z axis, either applied over a large volume by means of a *volume resonator* or over a specific volume of interest by means of a *surface coil*, as is the focus of this project.

With reference to the rotating coordinate system mentioned above, the applied $\mathbf{B}_1$ field will act to rotate the magnetic moment about its axis towards the xy plane, at a precessional frequency $\omega_1 = -\gamma\mathbf{B}_1$. Typically a short burst of RF energy is applied, the duration and intensity of which determines the extent of rotation. Of particular interest in MR applications are 90°pulses, which rotate the magnetization into the xy plane, and 180°pulses which effectively invert the spin system, leading to the reversal of spins relative to the rotating frame of reference.

The rotating component in the xy plane is the source of the MR signal, and may be detected by an appropriately aligned RF coil. It should be noted that only a very small proportion of spins (typically in the order of a few in 10^{-6}, as determinable by the Boltzmann distribution) participate in this process, and hence only a very small signal is observable. This explains why MRI is not a very sensitive technique, and places high demands on the detection hardware.

2.2.3 Relaxation Processes and The Bloch Equations

Whilst useful for understanding the MR phenomenon, the classical model presented here cannot explain many features relating to the interactions between nuclei. To overcome some such limitations, a set of phenomenological equations describing the dynamics of nuclear magnetization were proposed in [Bloch et al., 1946]. These Bloch equations describe processes of relaxation of the net magnetization. Various such relaxation processes arise which lead to a fading of the MR

signal after the initial excitation; these are largely dependent on the material and structure being observed, and as such their measurement allows characterisation of the materials.

2.2.3.1 Longitudinal Relaxation (T_1)

Longitudinal relaxation, also known as spin-lattice relaxation and represented as T_1 relaxation, describes the transfer of energy from the spin system, primarily through interactions with adjacent spins in the lattice. This is largely related to mobility and tumbling of molecules in the material – hence, the physical structure of the material and surrounding surfaces. The T_1 relaxation is defined by the Bloch equation

$$\frac{d\mathrm{M}_z}{dt} = \frac{\mathrm{M}_0 - \mathrm{M}_z}{\mathrm{T}_1} \tag{2.2.12}$$

2.2.3.2 Transverse Relaxation (T_2)

Transverse relaxation, also known as spin-spin relaxation and represented as T_2 is loss of *net* magnetisation from the xy plane. This is a result of loss of phase coherence due to small variations in the B_0 field (and hence, the local precessional frequency) due to the relationship between the nucleus and the molecular magnetic field, or exchange of spin state between two nuclei. In biological tissue, this process is significantly faster than longitudinal relaxation.

Transverse relaxation is described by the remaining Bloch equations,

$$\frac{d\mathrm{M}_x}{dt} = -\frac{\mathrm{M}_x}{\mathrm{T}_2} + \gamma \mathrm{M}_y \mathbf{B}_0 \tag{2.2.13}$$

$$\frac{d\mathrm{M}_x}{dt} = -\frac{\mathrm{M}_y}{\mathrm{T}_2} - \gamma \mathrm{M}_x \mathbf{B}_0 \tag{2.2.14}$$

In practice, the envelope of the FID is observed to decay at the *effective* T_2 relaxation time T_2^*, which is always faster than T_2. This has the added factor of phase loss due to macroscopic fluctuations due to magnetic field inhomogeneities;

$$\frac{1}{\mathrm{T}_2^*} = \frac{1}{\mathrm{T}_2} + \frac{\gamma \Delta \mathbf{B}_0}{2} \tag{2.2.15}$$

When a spin system which has been allowed to dephase for a short period is inverted (perhaps by way of a 180°pulse), the direction of rotation relative to the rotating frame of reference is reversed and the dephased spins begin to rephase. Effects from relatively static macroscopic inhomogeneities (defining T_2^*) are cancelled and an echo signal may be seen from the rephased spin system, attenuated at a rate determined by the T_2 component. It is generally this echo signal which is used to produce an image.

2.2.4 High field Strengths

In clinical applications, field strengths for the main magnet $\mathbf{B}_0$ are typically in the order of 1.5-3T. The smaller-scale animal research hardware being targetted in this project has a significantly higher field strength of 7T. The higher

field strength allows a substantial gains in signal-to-noise ratio (SNR) to be achieved, both due to an increased population of spins participating in the processes (determined by the Boltzmann distribution, and proportional to $\mathbf{B}_0$) and due to the increased rate-of-change-of-flux through the coil (relating to the higher ω_0). [Redpath, 1998] This in turn facilitates the acquisition of higher resolution images in shorter timeframes than with lower field strength hardware. However, the higher field strength introduces several challenges for hardware development, as discussed in [Kelley, 2006] and more broadly [Robitaille, Pierre-Marie and Berliner, La and may exacerbate certain imaging artifacts (for example, chemical shift artifacts).

2.2.5 Spatially Localised Nuclear Magnetic Resonance for Imaging

As noted above, the processional frequency of magnetic dipoles (the Larmor frequency) is proportional to the magnetic field strength acting upon that dipole. Hence it follows that by manipulating the magnetic field strength, it is possible to alter the frequency of an RF pulse to which the dipoles will respond en masse, and conversely the frequency of the received echo signal. Spatial localisation may be achieved by varying the magnetic field such that only a certain region responds to the pulse or produces a coherent echo at the nominated frequency, and it follows that an image may be constructed by sampling multiple different volumes across the total volume to be imaged. In MRI equipment, the required spatial variations in field are generated by gradient coils, with fields and RF pulses combined in various sequences to achieve the desired effect.

Spatial Encoding Gradient Coils MRI equipment typically employ a set of three orthonormal gradient coils (in the X, Y and Z planes) to superimpose a (nominally) linearly-varying field on the primary $\mathbf{B}_0$ field, resulting in a Larmor frequency which is a function of position. By applying different fields at certain stages between excitation and detection of the echo, it is possible to encode position in three axes discretely, as a function of frequency and phase within an activated slice. This principle is discussed in the context of imaging sequences, below. Assuming Nyquist criteria are met in the encoding stages (hence, no phase wrap or aliasing occur) the application of a two-dimensional inverse Fourier transform on the received signal from a particular encoded slice is sufficient to recover spatial information from the signal for rendering an image.

2.3 Pulse Sequences for Imaging

Various sequences of excitation and gradient pulses may be used to generate images, selected depending on the requirements of contrast and signal quality, highlighting or suppression of particular features, artifacts or tracing substances, handling of motion, constraints on scanning time and so forth. For the purposes of this project, two of the most basic imaging sequences are employed as detailed below:

2.3.1 The Spin-Echo (SE) Imaging Sequence

The spin-echo sequence is one of the most basic sequences used in magnetic resonance imaging. This sequence works as follows, with reference to figure 2.1.

1. An excitation pulse of magnitude and duration to produce a 90°rotation is applied at $t = 0$ in the presence of a slice-selection gradient, rotating the net magnetization in the selected slice to the transverse plane. The spins begin to dephase (as determined by T_2) and recover to normal orientation (described by T_1) immediately as the excitation is removed.
2. Immediately after the application of the excitation pulse, the slice-selection gradient is reversed to allow refocussing of the spins across the slice.
3. A momentary phase-encoding gradient is then applied, in the presence of a frequency-encoding gradient. This allows spins along the slice in the encoding direction to gain phase proportional to the position along the gradient.
4. A refocussing pulse corresponding to a 180°flip is applied at $t = \mathrm{TE}/2$, to reverse the spin direction. TE is the operator-defined *echo time*, chosen to give a particular contrast in the image (described in the following section). The inverted spins begin to rephase (cancelling the dephasing accumulated since the initial excitation), producing a measurable echo at TE as phase is recovered.
5. After a selected delay, at chosen *repetition time* $t = \mathrm{TR}$, the sequence is repeated. The delay allows for a certain proportion of spins to recover their orientation to the z direction, thereby allowing them to participate in the next excitation sequence (those remaining in the transverse plane will not be affected as desired by the 90°pulse).

The envelope of the received signal may be described by:

$$\mathrm{S} = \mathrm{M}_0 \left(1 - e^{-\frac{\mathrm{TR}}{\mathrm{T}_1}}\right) e^{-\frac{\mathrm{TE}}{\mathrm{T}_2}} \tag{2.3.1}$$

The spin echo sequence offers good signal to noise ratio and spatial resolution, and is less prone to certain artifacts than many other sequences. However, it tends to be slow and require higher levels of RF energy (hence has a greater specific absorption rate (SAR)) than alternatives.

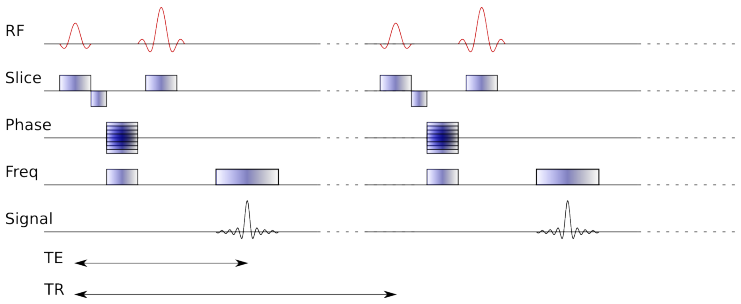

Figure 2.1: The basic Spin-Echo imaging sequence

2.3.2 Contrast and Weighting

Different materials have unique recovery characteristics, with different ratios between their T_1 and T_2 recovery rates. This allows for different contrast between materials to be achieved in an image, by varying the relative effect of T_1 and T_2 on the intensity of the generated image.

2.3.2.1 T_1 Weighting

T_1 weighting is typically achieved with short repetition time (typically slightly $< T_1$) and echo time ($<< T_2$). Equation 2.3.1 then simplifies to

$$S \approx M_0 \left(1 - e^{-\frac{TR}{T_1}}\right) \tag{2.3.2}$$

The short repetition time allows for somewhat faster scans.

2.3.2.2 T_2 Weighting

T_2 weighting is achieved with a long repetition time (usually several times $> T_1$) and a moderate echo time (typically between the longest and shortest material T_2 of interest). Equation 2.3.1 then simplifies to

$$S \approx M_0 e^{-\frac{TE}{T_2}} \tag{2.3.3}$$

In the case of a gradient echo sequence, where there is no additional refocussing pulse, this combination actually gives a T_2^* weighted image.

2.3.2.3 Spin Density Weighting

Spin density weighting offer no particular highlighting of T_1 or T_2 decay, instead giving a signal describing the population density of spins (protons) in the material. This may be achieved with a short echo time and long repetition time.

2.3.3 The Gradient Echo (GE) Sequence

The gradient echo sequence as illustrated in figure 2.2 operates in a similar way to the spin echo sequence, although uses bipolar gradients rather than an inversion pulse to achieve refocussing and echo generation. Generally smaller flip angles (for example, 30°) are used than in a spin echo sequence; this means that less signal will be available for image generation, but allows residual z magnetization to be consumed in subsequent excitations – thereby allowing sorter repetition times and faster image acquisition. Although z magnetization does not fully recover due to the short repetition time, an equilibrium is established after the first few excitations. Gradient echo imaging generally allows faster acquisition with lower SAR than spin echo sequences, albeit somewhat more vulnerable to certain artifacts (including those due to field inhomogeneities). Variations on the sequence allow improvements in terms of signal strength, artifact reduction, imaging time and measurement of flow.

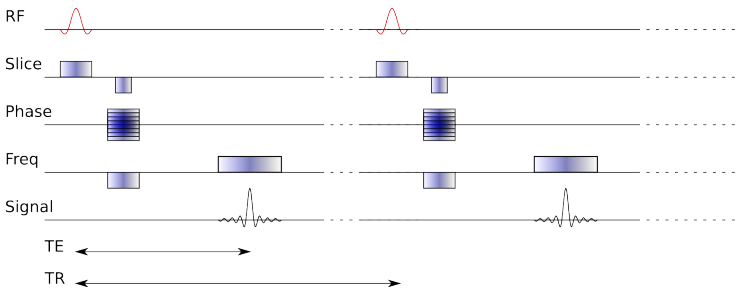

Figure 2.2: The Gradient Echo imaging sequence

2.4 RF Coil Design for Magnetic Resonance Imaging

The RF coil in a MRI system is responsible for transmission of the excitation and refocussing pulses (90°and 180°) into the object being imaged. Additionally, an RF coil is used to listen for the echo produced from rephasing of the spins following the initial RF pulse. RF coils may be designed to cover a large volume encompassing entire objects with good $\mathbf{B}_1$ homogeneity (these are categorised as *volume coils*), or they may focus the RF power on a particular volume of interest in the object, normally near to the surface of the object where the coil may be mounted. The latter type are referred to as *surface coils*, and are the focus of this project and all further discussion. It is noted that it is not necessary to use the same coil for transmission and reception, and a combination of surface and volume coils may be used in some situations.

When compared with volume coils, surface coil designs allow placement of the coil and concentration of the field in a region much closer to the object being imaged; this typically leads to significant improvements in signal strength and hence signal to noise ratio in a small region, although at the expense of homogeneity in the image. In this section, basic tools useful to understanding the design of a surface coil are presented, which will later be referenced in the context of the coils being implemented.

2.4.1 Electromagnetic Response and the Biot Savart Law

A key feature of a surface coil is of course the distribution of the magnetic field which it produces; this determines the penetration depth to which the coil may be used effectively for imaging, the homogeneity to be expected from produced images, the proportion of the energy being delivered to the object and the volume over which noise may be received.

The behaviour of electric and magnetic fields, their interrelation and dependence on charge and current density are described by the aforementioned Maxwell Equations. One result of these equations, taking magnetostatic approximations, is the Biot Savart law which describes the magnetic field $\mathbf{B}$ generated by an electric current I as:

$$\mathbf{B}(\mathbf{r}) = \frac{\mu_0 I}{4\pi} \int_C \frac{d\mathbf{l}' \times \mathbf{R}}{R^3} \tag{2.4.1}$$

The field at a particular point from a given coil may therefore be approximated by integrating over the coil geometry. [Jin, 1999]

It should be noted that the Biot Savart Law is an approximation assuming a *constant* current; furthermore, in many design applications a simplification of the real geometry is applied for the integration (for example, assuming conductor elements to be infinitesimally thin). Nonetheless, it provides a suitable starting point for evaluating the general form of the field and selecting coil geometries, which may then be refined by more advanced methods (for example, full-wave numerical analysis using the Method of Moments or Finite Difference Time Domain method).

2.4.2 Tuning and Matching

In order to be effective for imaging, the RF coil must be tuned to resonate at the Larmor frequency f_0 of the nucleus to be detected. This is typically achieved by adding capacitive or inductive elements across or along the coil structure.

Also of great significance is the interface between the coil and the RF hardware of the MRI machine. In order to minimize losses, optimize power transfer to the coil and suppress reflected signals which may degrade the image, it is necessary that the impedance of the RF power amplifier (source), the receiver preamplifier, the cable connecting the coil, and the load presented at the end of the cable are all matched. [MacLaughlin, 1989, Bowick, 1997]

To achieve these goals, it is helpful to devise a circuit model to describe the behaviour of the coil, associating its physical characteristics with basic equivalent circuit elements. From this model, the requirements in terms of additional tuning or matching components may be determined. This is detailed in section 5.2.2

2.4.3 Quality (Q) Factor

The 'precision' of tuning – the frequency selectivity of the received coil – may be described by the Q factor. This may be calculated in various ways depending on context, but generally relates the peak magnetic energy stored by the coil to the average energy dissipated per radian. Equivalently, it may be expressed as the ratio of the reactive impedance over the resistive impedance ($Q = \omega_0 \frac{L}{R}$) or the frequency bandwidth over the center frequency ($Q = \frac{\mathrm{B_{3db}}}{f_0}$). [Barral, 2009]

2.4.4 High-field Considerations

The shorter wavelengths and penetration depths associated with higher field strengths and proportionally higher ω_0 complicated the design of coils. The exact $\mathbf{B}_1$ field distribution becomes more difficult to calculate accurately, as does the interaction of this field with tissue; for these purposes, modelling and computation by way of the Finite Difference Time Domain (FDTD) method is commonly required. This is discussed in detail in [Collins, 2006].

Higher operating frequencies put additional constraints on the RF hardware and coil conductors – for example, with conductor lengths over about one tenth of the wavelength, phase differences across the conductor may give rise to destructive interferences and loss of signal as discussed in section 5.2.4.2.

2.4.5 Additional Features

There are several was in which the basic behaviour of the RF coil may be extended for improved performance or specialised applications. Although not a focus of the work undertaken here, these are mentioned briefly for completeness, and identified as possible extensions to the implementation performed.

Quadrature detection adds an additional receive channel, operating along an orthogonal axis in a volume overlapping the first channel – thereby recording a 'real' and 'imaginary' component for the received signal. This produces a better signal-to-noise ratio in the received image.

Active decoupling is used when different coils are to be used for transmitting and receiving. In this case, mutual coupling between two tuned coils in the system may degrade the signal and generate artifacts; furthermore it is possible that strong transmitted signal could saturate the receiver in some hardware configurations, possibly requiring some time for recovery. An actively decoupled coil uses a trigger signal generated from the scanner to momentarily detune the receive coil during RF pulse transmission, thereby avoiding these effects. This is often accomplished with a PIN diode switch in the tuning circuitry, which provides a high resistance (and low parallel capacitance) when reverse-biased by the trigger signal and a low resistance when forward-biased.

Double tuning may be helpful for imaging isotopes which are expected to generate a relatively low signal level. In these situations, the response from the isotope of interest may be inadequate for generating a good signal, either for an initial 'pilot' image suitable for calibrating a scan or for the acquisition itself. This is solved by combining coils for such isotopes with a ^{1}H coil with an overlapping imaging area (often concentrically placed, in the case of a simple loop). This ^{1}H coil may be used to generate a stronger signal suitable for calibrating the scan geometry for the other isotope, to stimulate magnetization transfer to the isotope of interest or to decouple proton signals in MRS experiments.

Coil arrays are used to obtain specialised response patterns – perhaps providing a stronger response or more uniform signal in a particular area of interest than a single coil. This can also help to limit the specific absorption rate (see section 2.6.2) by focussing more of the energy where it is required. Generally components of the array need to be tuned and matched with respect to one another and to the receiver, making this arrangement somewhat more complicated to implement. In some cases (where supported by the scanner hardware) elements of the array may be connected to separate transmit/receive channels, with the response later combined as a post-processing stage.

2.5 Physical Design and Material Selection for MR applications

Since the coil is to be operating in a very strong magnetic field, it is important that all components contained within are "non-magnetic". Special consideration has to be given to housing of the equipment, the coaxial line and its terminations, the coil material, and component materials and their termination (for tuning and fixed capacitors, for example). Even relatively small quantities of moderately magnetic materials will be subject to significant force in the vicinity of the magnet, making secure mounting difficult and potentially turning them into projectiles – posing a significant safety risk. Even lesser quantities not leading to significant kinematic force may create perturbations in the main field which could be manifest as artifacts in the resulting image. Hence, it is important to select materials known to have a low magnetic susceptibility – weakly diamagnetic materials as described in table 2.1 are generally acceptable, although common component termination materials containing alloys of nickel, manganese and zinc with mass susceptibilities in the order of several thousand are problematic. Specialised capacitors and trimmer capacitors with non-magnetic terminals, plates, dielectric material and housing must be used. Ferromagnetic inductor cores must of course be avoided, although generally for RF applications air cores are preferred for their lower loss and higher Q anyway. Coaxial cables must be specially selected, and attention must be given to interconnecting wires, including the conducting core and any coating. Attention must also be given to the solder used (ensuring no troublesome additives), any other chemical treatment used in manufacture (for example, ferric chloride etchants), and all mounting hardware used throughout.

Material	Mass Susceptibility χ_{mass} $(\times 10^{-8} m^3 \cdot kg^{-1})$
Copper	-0.107
Aluminium	+0.82
Silver	-0.25
Perspex	-0.5
PVC	-0.75
H_2O	-0.90
$CuSO_4 \cdot 5H_2O$	+ 7.7

Table 2.1: Mass Susceptibility of various materials [**?**]

2.6 Aspects of Image Quality

2.6.1 Sensitivity and Signal to Noise Ratio

Since the echo signal available will be very small, the sensitivity of the coil when receiving is critical to obtaining a good image. In particular, a key design goal is to maximise the signal to noise (SNR) ratio of the resulting image.

Noise in the image arises from a number of sources; one of the more significant (and immutable) of these is thermal noise. Thermal noise may be described by the fluctuation dissipation theorem, which gives the Root Mean

Squared (RMS) noise voltage as

$$v = \sqrt{4k_B T_S R \Delta f} \tag{2.6.1}$$

where R is the total resistance of the loaded coil and Δf the bandwidth of the received signal.

The potential achievable signal to noise (SNR) ratio of a coil can be estimated by the induced EMF in the coil, over the thermal noise. The induced EMF is determined by Faraday's law [Barral, 2009]

$$\xi = -\frac{\delta\theta}{\delta t} \tag{2.6.2}$$

$$\propto -\frac{\delta\left(\mathbf{B}_1\mathbf{M}_0\right)}{\delta t} \text{ [Hoult and Richards, 1976]} \tag{2.6.3}$$

where θ is the magnetic flux across the coil. Magnetization may be given as,

$$\mathbf{M}_0 = \frac{N\gamma^2\left(\frac{h}{2\pi}\right)^2 s(s+1)\mathbf{B}_0}{3k_B T_s} \tag{2.6.4}$$

$$= \frac{\sigma_0\mathbf{B}_0}{\mu+0} \tag{2.6.5}$$

where N is the number of nuclear spins s per unit volume ($s = \frac{1}{2}$ for protons) and T_s is the temperature of the sample. Since $\omega_0 = \gamma\mathbf{B}_0$ it follows that $\xi \propto \omega_0^2$.

$$\text{SNR} = \frac{\xi}{v} \tag{2.6.6}$$

There may also be a lesser contribution from shot noise (not dealt with here) and electromagnetic interference (which may generally be suppressed by adequate shielding).

Signal-to-noise visible in a generated image may be improved by a number of means, as summarised in table 2.2. Nonetheless, all of these are dependent on the underlying SNR offered by the coil and imaging hardware.

Parameter	Consequences
Increase number of exposures	Increased scan time
Decrease matrix size	Decreased Resolution Decreased scan time
Increase slice thickness	Decreased resolution
Decrease receive bandwidth	Minimum TE increased Chemical shift artifact increased
Increased field of view	Decreased resolution
Increase TR	Image contrast/weighting changed (reduced T1) Increased number of slices
Reduce TE	Reduced T2 weighting

Table 2.2: Maximising the received Signal to Noise ratio – tradeoffs

2.6.2 Specific Absorption Rate (SAR)

Particularly when performing in-vivo scans, and in situations where excessive heating of the object may be problematic, it is also important to consider the Specific Absorption Rate (SAR), the rate at which energy will be absorbed by the object mass. It can be shown that:

$$\mathrm{SAR} \propto \frac{\sigma_{sample}}{2\rho_{dty}} E^2 (1 - Q_{ratio}) \left[\frac{W}{kg}\right] \tag{2.6.7}$$

This is not sufficient to obtain an absolute value, but may be used in this context as the basis for comparison. [Barral, 2009] In particular, the dependence on sample loading and Q factor is notable.

While surface coils with their more concentrated field allow for a lower SAR over the body as a whole (since only a small region of interest is excited, and generally less energy over a shorter time is needed to accumulate comparable signal), they may introduce issues with *local* SAR in the imaging area which receives a more intense signal.

2.6.3 Imaging Artifacts

Imaging artifacts are defects in the generated image, either in terms of geometry or intensity. These may arise from limitations of or defects in the imaging hardware, from inappropriate selection of imaging parameters, from movement of the object to be imaged or from certain characteristics of the object itself. For example, a slight change in Larmor frequency in different media may cause a geometric shift of certain objects in an image; this is known as a *chemical shift artifact*. Motion of the subject or fluid transport can introduce geometrical or intensity variations. Specially designed pulse sequences or respiratory or cardiac gating may be used to suppress (or in cases where flow is of interest, enhance) these effects.[Westbrook et al., 2005]

Radiofrequency interference (RFI) may give rise to noise, spikes or lines (*zipper artifacts*) in the generated image due to inadequate shielding of components in the RF system. Inhomogeneities in the magnetic will create fluctuations in intensity, and sudden changes in the local magnetic field (for example due to pronounced differences in susceptibility of materials) may give rise to further geometric distortion and shading. Aliasing, wraparound and ghosting occur when anatomy from outside the nominated field-of-view is folded on top of anatomy within the field of view, possibly due to violation of the Nyquist sampling criteria when encoding or due to deficiencies in the RF coil design or implementation.

Part II

Materials, Methodology, Implementation

Chapter 3

Tools and Materials

3.1 Target Hardware

The coil is developed for use with 7 Tesla (T) MRI equipment. Although the interface and parameters are broadly compatible across various models and vendors (hence, similar operation and performance could be expected on any 7T hardware), the current design is specifically intended to fit a Bruker Biospec Avance 70/20AS small animal scanner described in section 7.6. This sets constraints in terms of physical dimensions (120mm internal diameter) and power handling (500W), with impedance (50Ω) being somewhat standard and operating frequency being determined by the field strength and nucleus of interest.

3.2 Design Tools

Parametric evaluation is performed with custom programs developed in MATLAB from the MathWorks (http://www.mathworks.com/products/matlab/).

Electronic simulation and optimisation of the device is performed using a circuit model implemented in SPICE. The free LTSpice application from Linear Technologies (http://www.linear.com/designtools/software/ltspice.jsp) is used for this purpose.

Full-wave electromagnetic simulation and visualisation is performed using the FEKO suite (http://www.feko.info/).

PCB layout is performed using GNU PCB (http://pcb.gpleda.org/)

Additional software associated with acquisition and evaluation of images from the MRI scanner is detailed in section 7.7.4.1.

3.3 Fabrication

Coils are tune-and-match circuitry are assembled using standard electronic assembly tools; careful attention must be given to the quality of the solder joins and to the complete removal of enamel coating from the endpoints of the coil wire (where applicable) as any inadequacy in this regard will degrade the performance. Leaded solder is often preferred for these applications where available, due to its better characterised behaviour (although it was not used in this work due to RoHS restrictions).

Printed circuit boards (where used) are transferred by standard photographic processes onto 0.035mm copper-clad FR4 board with photoresistive coating, using the processing facilities at the Institutt for Teknisk Kybernetikk (ITK). This involves an opaque printing of the copper mask pattern onto transparent film (laser printer toner is generally adequate), transfer onto the circuit board by ultraviolet (UV) illumination of the photoresistive coating through the printed mask, followed by chemical fixation and etching. The areas shaded from the UV illumination acquire a resistance to the etchant during this process, whilst those exposed to UV illumination have no such resistance. Hence, copper from transparent regions of the original mask is removed from the board, whilst copper from the opaque areas (corresponding to the PCB traces) remains.

As the standard $FeCl_3$ etchant used in this process gives rise to strongly paramagnetic biproducts, it is necessary to be particularly careful when cleaning the board to avoid the possibility of introducing inhomogeneities or imaging artifacts due to residue on the board itself.

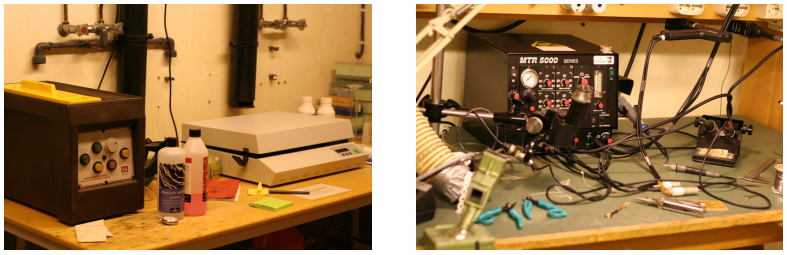

Figure 3.1: Fabrication facilities

3.4 Characterization and Tuning

An initial estimate of the response of the coil and tune-and-match circuitry may be evaluated by software simulation and calculations from a model; nonetheless, particularly when operating at high frequencies, various additional sources of loss and parasitic effects appear in any physical implemenation. For this reason, the implementation will generally require iterative adjustment depending on particulars of the individual construction.

Initial tuning of the coil requires feedback from a network analyzer; this device is also used for assessing the broad frequency response of the device,

and estimating the response characteristics of the coil as detailed in section 7.7.3.

3.5 Evaluation

Meaningful evaluation of the coils is best performed on the actual instrumentation where they will be used, in situations closely resembling a real imaging scenario whilst still providing measurable data. To this end, evaluation data will be collected using a 7T small animal scanner. Initially, imaging will be performed on phantoms with known, stable characteristics suitable for numeric assessment of the image quality. Subsequently, imaging of biological matter will be performed for visual comparison. Detailed specification of the scanner and the phantoms in use is provided in the evaluation section 7.6.

Chapter 4

Methodology

4.1 Overview

Coil development took place in a number of stages; initially, a simple loop surface coil was developed for ^{1}H MRI. In addition to the primary outcome of producing an application-specific coil, this served as a means to develop and refine design and testing procedures in preparation for the more challenging task of developing a coil arrangement suitable for imaging a live fish.

The design process consisted of an initial phase of research, parameter definition and software modelling of the electronic and electromagnetic properties of the coils and associated tuning components. This software model was used to optimise initial component values and circuit layout, prior to fabrication of a prototype.

Initial validation and tuning of the prototype was performed with a network analyzer outside of the magnet, and finally the prototype was placed in the magnet along with various phantoms, to assess performance in a real imaging situation.

4.2 Design Process

4.2.1 Electromagnetic Design and B_1 Field

It is intuitive that $\mathbf{B}_1$ inhomogeneity is a major cause of artifacts in MR imaging modalities. In standard spin echo experiments, inhomogeneity is observed as loss of signal, hence degraded SNR. [Zelaya et al., 1997].

The signal-to-noise performance of a coil can be improved by reducing the noise volume, which is made possible by placing the coil much closer to the object being imaged; this is one of the basic premises behind the use of surface coils. The reduction in noise volume generally comes at the price of an inhomogeneous $\mathbf{B}_1$ field, and hence non-uniformity in the image intensity.

The transmitted $\mathbf{B}_1$ field may be described with the help of the Biot Savart law, presented in section 2.4.1. It follows by reciprocity that the spatial sensitivity of reception will be the same as the transmitted $\mathbf{B}_1$ field. As described in the earlier section, evaluation of the Biot Savart law can become very complex, and this type of modelling is best accomplished with software simulation.

Nonetheless, for simplified geometries exhibiting some degree of symmetry as will be dealt with here it is relatively easy to derive a useful expression for the field along an orthogonal line through the central axis of the coil. For example in the case of a single circular loop the field along the z axis may be described by [Jin, 1999]:

$$\mathbf{B} = \mu_0 I \frac{a^2}{2\left(a^2+z^2\right)^{\frac{3}{2}}} z \tag{4.2.1}$$

Off-axis response may be simulated in software, for example using the Feko software suite (section 3.2).

4.2.2 Electronic Design

As discussed in the introductory section 2.4.2, it is necessary that the coil itself may be tuned to have a resonant peak corresponding with the Larmor frequency f_0 of the nuclei to be imaged (detailed in section 2.2.1); this is achieved by cancelling the reactive component of the coil impedance. Furthermore, impedance at f_0 must be matched to that of the transmitter (typically 50Ω) to ensure optimal power transfer and signal quality and minimise the noise factor of the receiver. [Bowick, 1997]

To determine the frequency response of the coil and develop an appropriate tune-and-match configuration, an 'equivalent circuit' model is used to represent the coil itself, with tune and match components chosen accordingly. The equivalent circuit model and corresponding tune-and-match circuit may be analyzed numerically; a simple Matlab script evaluating model components is used for this purpose. The behaviour may also be simulated using standard circuit simulators; during this work LTSpice (see section 3.2) is used for this purpose. In the Spice simulator it is possible to visualise the effects of altering particular parameters, in terms of signal strength and Q factor of the circuit. It is also possible to verify the tuning range and matching abilities of the chosen components for a particular coil geometry.

4.2.2.1 Q estimation

The Q factor for the coil may be estimated in terms of the equivalent circuit elements as [Edelstein, 2006]

$$Q = \frac{\omega L_{total}}{R_{total}} \tag{4.2.2}$$

4.3 Prototyping

Following initial design and simulation, circuits are constructed physically based on parameters calculated from the model. These are then attached to a network analyzer to verify their frequency response. Finally, the coils are attached to the MRI scanner and placed in the bore, where frequency response, tuning and matching are again verified. From this point, evaluation as described in section 7 may proceed.

4.3.1 Tuning and Matching

With a network analyzer in forward reflection (S11) mode (see section 7.6.3), capacitor values are adjusted such that the tunable band covers the desired range (in the close vicinity of 300MHz, as shown in figure 4.1a) for the loaded coil. This may require substitution of the modelled fixed capacitor with another of slightly different value.

Parallel (tuning) capacitance is then adjusted such that resistance at ω_0 is near to 50Ω; this is not necessarily exactly at the resonant peak [Barral, 2009]. This is performed on the network analyzer, in S11 mode with either a log magnitude display (as in figure 4.1b) or smith chart format as illustrated in figure 4.1c. Here, the cursor is at ω_0 and the circle intersecting the center of the plot represents a 50Ω contour. Once this has been determined, the matching capacitor is adjusted for optimal signal.

The reflection coefficient S11 represents

$$\mathrm{S11} = \Gamma = \frac{Z_L - Z_0}{Z_L + Z_0} \qquad (4.3.1)$$

where Z_0 is the reference impedance (50Ω). Coil impedance is hence given by:

$$Z_0 = 50 \cdot \frac{1 + S11}{1 - S11} \qquad (4.3.2)$$

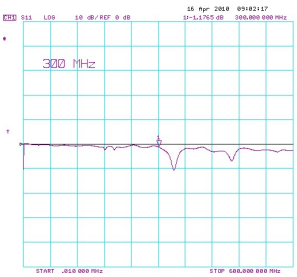

(a) Starting point for tuning the coil, S11 log magnitude over a broad frequency range

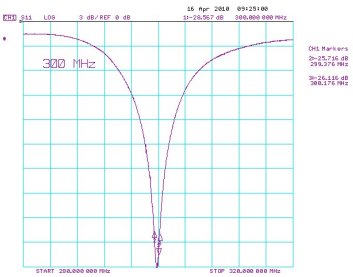

(b) Response of the tuned coil, S11 log magnitude over a narrow band

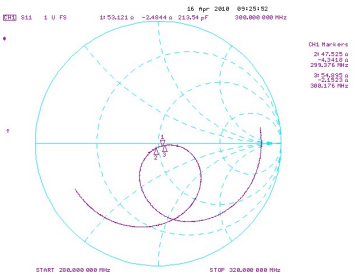

(c) Matching the coil on the smith chart; the circle intersecting the center of the image corresponds with a 50Ω match.

Figure 4.1: Tuning and matching a coil using the network analyzer

4.4 Evaluation

Evaluation of the implementations is detailed thoroughly later in section 7.

Chapter 5

Small Loop ^{1}H Surface Coils

5.1 Introduction

The initial design goal in this project was to develop a basic surface coil for ^{1}H proton MRI, suitable for imaging the brains of rats (with application to study of tumor development). For this purpose, circuit models for describing multi-turn wire loops and flat 'washer' geometries were devised and evaluated. Comparing the various arrangements, a single-loop wire element was found to be most favourable to the requirements. This configuration was investigated in depth and three hardware revisions were constructed, two of which are evaluated fully in later stages.

5.2 Methodology

5.2.1 Basic Geometry

For imaging a rat brain, a target depth in the vicinity of 15mm is desirable; this corresponds to a loop radius in the area of 11mm for optimal SNR performance – as interpolated from results determined by electromagnetic simulation performed in [Kumar et al., 2009], for SNR-optimised target depth at 7T.

5.2.2 Circuit Model

To characterise the electrical behaviour of a particular loop, an equivalent circuit model is used describing the intrinsic resistive, inductive and capacitive elements of the conductor and the loop structure. The basic circuit model used to represent the coil is presented in figure 5.1, with parameters determined by specifics of the geometry, materials and loading conditions. This is similar to various models proposed in [Edelstein, 2006, Kumar et al., 2009, Loudet, 2009]; derivation of parameters is detailed in these references. In this diagram,

- $\mathrm{L_{loop}}$ describes the inductance of the wire loop
- $\mathrm{L_{wire}}$ describes the self-inductance of the wire making up the coil
- $\mathrm{C_{loop}}$ represents the lumped capacitances in the loop structure

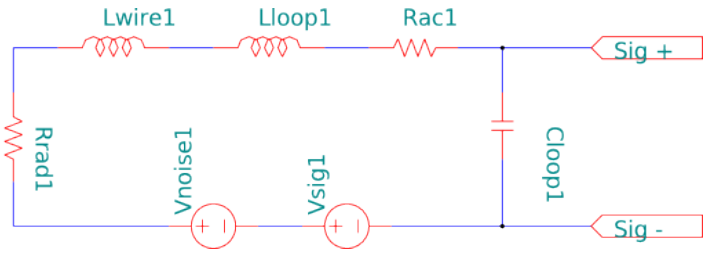

Figure 5.1: Basic circuit model for a single resonant RF coil

- $\mathrm{R_{AC}}$ describes the AC resistance in the coil, due to the skin effect
- $\mathrm{R_{rad}}$ describes the radiation resistance of the sample

AC resistance arises as a result of the skin effect, and is a function of frequency. Eddy currents set up by the rapidly alternating current tend to create a current distribution such that the current density towards the surface of the conductor is significantly greater than that towards the center. The depth at which the current density decays to about e^{-1} is termed the *skin depth* and is given by: [Sadiku, 2001]

$$\delta = \sqrt{\frac{2\rho}{\omega\mu}} \tag{5.2.1}$$

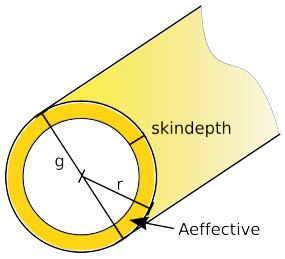

Figure 5.2: Skin depth

For a wire of circular cross-section and gauge significantly greater than δ, the resistance is approximately equivalent to the direct current resistance of a hollow tube of wall thickness δ, or

$$R \approx \frac{L\rho}{\pi\left(r^2 - (r-\delta)^2\right)} \tag{5.2.2}$$

where r is the cross-sectional radius of the conductor. This is illustrated in figure 5.2.2. In some designs, hollow tubes are preferred over solid conductors, offering comparable resistance with less mass.

In this instance, a solid copper conductor is chosen for its good conductivity, malleability, magnetic properties and availability. Aluminium may also be an appropriate conductor in some contexts, although it offers slightly lower conductivity and may be more susceptible to mechanical fatigue when worked into a coil form – it is perhaps better suited to a rigid 'washer' geometry. Defining the operating frequency as $f_0 = 300\mathrm{MHz}$, physical and material properties are determined as below, with skin depth δ from equation 5.2.1:

$$\begin{aligned}
\sigma_{sample} &= 377\Omega \text{ (free space)} \\
\rho_{\mathrm{Cu}} &= 1.678 \times 10^{-8}\Omega\mathrm{m}^{-}1 \\
\mu_0 &= 4 \times 10^{-7}\pi\mathrm{Hm}^{-1} \\
\mu_{Cu} &\approx \mu_0 \\
\omega &= 2\pi \cdot 300 \times 10^{6}\mathrm{Hz} \\
\delta &= \sqrt{\frac{2\rho_{\mathrm{Cu}}}{\omega\mu_{Cu}}}
\end{aligned}$$

5.2.2.1 Multi-turn wire geometry

For a coil consisting of multiple turns, elements of the equivalent model may be described as [Loudet, 2009, Bowick, 1997, Sadiku, 2001]:

$$\begin{aligned}
\text{Defining w as the winding length} \\
\text{d as the coil diameter} \\
\text{N as the number of turns} \\
\text{g as the wire gauge} \\
\text{l as the wire length}
\end{aligned}$$

$$\mathrm{L}_{\mathrm{loop}} = 8 \times 10^{-7} N^2 d \left(\log(\frac{\sqrt{2}dN}{w(N+1)}) + .37942 + \frac{1}{3}\left((N+1)\frac{w}{dN}\right)\right) \tag{5.2.3}$$

$$\mathrm{L}_{\mathrm{wire}} = 8 \times 10^{-7} N d \left(2.303 \log \frac{16d}{g} - 0.75 + 8Ndg \right) \tag{5.2.4}$$

$$\mathrm{C}_{\mathrm{loop}} = 3.9685 \times 10^{-13} * \left(\frac{\left(\frac{400d}{\pi}\right)^4}{100Nd} \right)^{\frac{1}{3}} \tag{5.2.5}$$

$$\mathrm{A}_{\mathrm{loop}} = \pi \left(\frac{d}{2}\right)^2 \tag{5.2.6}$$

$$\mathrm{A}_{conductor} = \pi \left(\frac{g}{2}\right)^2 \tag{5.2.7}$$

$$\mathrm{A}_{\mathrm{effective}} = \mathrm{A}_{conductor} - \pi \left(\frac{g}{2} - \delta\right)^2; \tag{5.2.8}$$

$$\mathrm{R}_{\mathrm{AC}} = \frac{l\rho_{\mathrm{Cu}}}{\mathrm{A}_{\mathrm{effective}}} \tag{5.2.9}$$

$$\mathrm{R}_{\mathrm{rad}} = \frac{8}{3}\sigma_{sample}\pi^3 \left(\frac{N\mu_0 \mathrm{A}_{\mathrm{loop}}}{\lambda^2} \right)^2 \tag{5.2.10}$$

It is also possible to take into consideration lift-off of the coil from the sample, as proposed in [Suits et al., 1998]:

$$\mathrm{R_{rad}} = \left(\frac{2}{3\pi}\right)\left(\mu_0^2 N^2 \omega^2 \sigma_{sample} r^3 \mathrm{atan}\left(\frac{\pi r}{8h}\right)\right) \tag{5.2.11}$$

Where h is the liftoff from the sample.

5.2.2.2 Washer geometry

An alternative to a wire loop is to construct a flat 'washer' geometry, perhaps etched onto a circuit board or formed from copper foil. This geometry is modelled in detail in [Kumar et al., 2009], and was implemented in Matlab for comparison purposes in this project.

5.2.2.3 Single-turn geometry

For evaluation of single-loop coils, the loop inductance can be characterised more simply by:

$$\mathrm{L_{loop}} = \frac{\mu_0 d}{2}\left(\log\left(\frac{8d}{g}\right) - 2\right)$$

Other parameters are evaluated using the same equations as for the multi-turn geometry described above, with N=1.

5.2.2.4 Simplifications in the Circuit Model

The circuit model above neglects various effects which appear in real (non-ideal) components and connections, and may become significant at high frequencies. These must be considered and mitigated during construction, and account for discrepancies between the modelled behaviour and that observed in a practical implementation.

Parasitic capacitances and inductances arise from PCB traces and interconnects between components; all conducting elements have an associated inductive component, and inductive coupling or parasitic capacitances may arise between nearby conductors. These often do not lead to energy loss per se, but do alter the response of the system. These effects may be minimised by ensuring that connections between components are short and well spaced or appropriately orientated relative to one another. Of particular note in these designs are the leads between the tune-and-match components and the actual loop, where relatively long, somewhat close and parallel conductors may be necessary but will introduce these effects.

Resistive losses arise for all interconnects (wires, PCB traces), all 'real' components and every solder join encountered. These are mitigated by keeping conduction paths short, and avoiding redundant joins.

Real capacitors have not only the key capacitative element, but also a series resistance (accounting for power dissipation in the element), a parallel (leakage, insulation) resistance, and a series inductance from the leads and plates. The combined equivalent of the resistances gives a frequency dependent *effective series resistance* (ESR). As frequency increases, at some point this series resistance and the inductive component become resonant, after which increasing frequency will see the 'capacitor' exhibit inductive behaviour. The ESR of a capacitor is largely dependent on the dielectric material, and may be described by the Q factor given by $Q = \frac{X_C}{ESR}$.

Proximity Effects may also increase the effective resistance of a wire at high frequencies, by reducing the effective conducting cross section in much the same way as with the skin effect. Proximity effects arise when parallel wires in close proximity induce eddy currents in one another, causing the current to concentrate on the side near the adjacent wire. This can become a problem when the conductor gauge is too large (hence, the internal diameter of the loop presented by the conductor edge is small).

5.2.3 Tuning and Matching

The purpose of the tune and match circuit is twofold. Firstly, it is used to tune the resonant peak of the loop to the required frequency. Secondly, it must cancel the reactive components from the coil impedance and present an appropriate load to the transmitter.

Taking the circuit model above, an expression for the impedance presented by the coil is described by:

$$Z = R + jX \tag{5.2.12}$$

$$= (\mathrm{R_{rad}} + \mathrm{R_{ac}}) + \frac{1}{\frac{1}{j(\mathrm{L_{loop}}+\mathrm{L_{wire}})\omega} + jC\omega} \tag{5.2.13}$$

Resonance occurs when

$$\mathrm{L_{total}C_{comp}}\omega^2 = 1 \tag{5.2.14}$$

Various options are present for tune-and-match circuitry. One very common configuration is to use an L-section (series-parallel) matching network, with purely capacitive networks. This configuration is relatively easy to design and model, and can be implemented with off-the-shelf non-magnetic components. A combination of capacitive and inductive elements often provides superior results and more flexibility in terms of tuning and matching capabilities, although this would require construction of customised fixed and variable inductors, which present various additional challenges in terms of physical construction and accurate modelling. Additionally, preliminary simulation of this configuration indicated that achieving the required inductances and acceptable tolerances with physically realisable non-magnetic components may not be possible. For these reasons, a variation on the two-element capacitive circuit was used for initial designs in this project as shown in figure 5.3. In this circuit, $\mathrm{C_{comp}}$ is selected to compensate for most of the reactive part of the coil

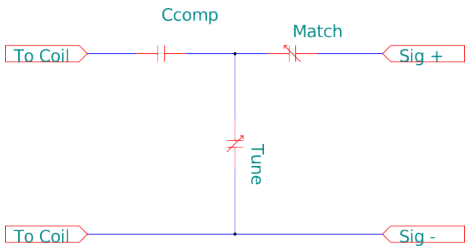

Figure 5.3: Tune-and-match circuit

impedance, with the *tune* and *match* variable capacitors serving to allow fine adjustments of this.

It is noted however that the two-element network has one key drawback, in that once the source and load impedances are determined by design, the Q of the network is also defined purely as a function of these – that is, there is no choice of circuit Q. In RF coil design it is often desirable to have a very selective high Q network, to maximise the signal to noise ratio and received image quality. Use of a three-element Π or T network would allow more control over the Q factor of the circuit, and could provide additional flexibility in terms of tuning and matching capabilities (albeit perhaps with slightly more loss due to additional components). [Bowick, 1997, Viohl and Gullberg, 2005].

5.2.4 Coil Design

The circuit model presented here was implemented in LTSpice, with equivalent circuit parameters and initial values for the tuning capacitors generated automatically from a Matlab implementation of the above equations. The corresponding models and scripts are contained on the CD accompanying this document, with a sample model and output presented in figure 5.4. Various assays made covering realisable designs (in terms of available materials, size and practicality constraints). It was determined that a single-turn wire loop implementation provided the most suitable response and Q factor.

5.2.4.1 Wire Gauge

There are several considerations in selecting the wire gauge. Wire which is too thin will have an increased impedance, resulting in loss of signal. Furthermore, the comparatively small volume and surface area gives a reduced ability to dissipate any heat resulting from losses in the coil – potentially leading to excessive heating of the element. Additionally, a thin wire element may not be sufficiently robust to maintain its form during normal handling. Conversely, too large a gauge may be difficult to work into the desired form, and could introduce additional proximity effects. A 1.62mm gauge copper conductor was selected to provide a reasonable tradeoff between these factors.

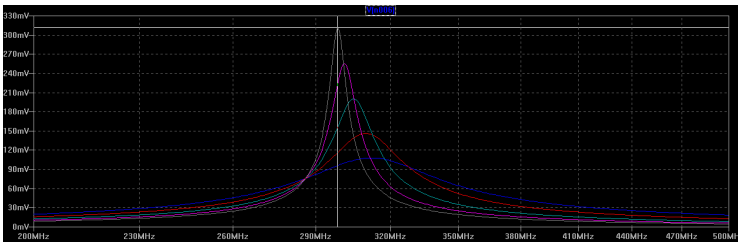

(a) Tuning the coil; Ctune swept from 1 (lower right) to 20pF (upper right)

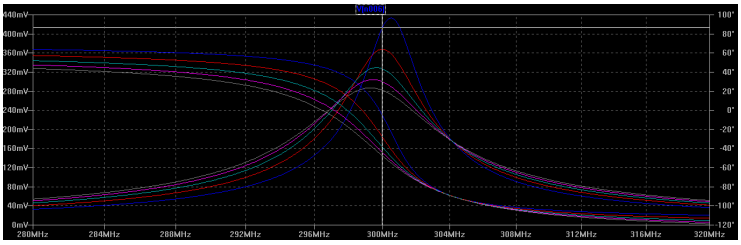

(b) Matching the coil; Cmatch swept from 8 (lower left) to 14pF (upper right)

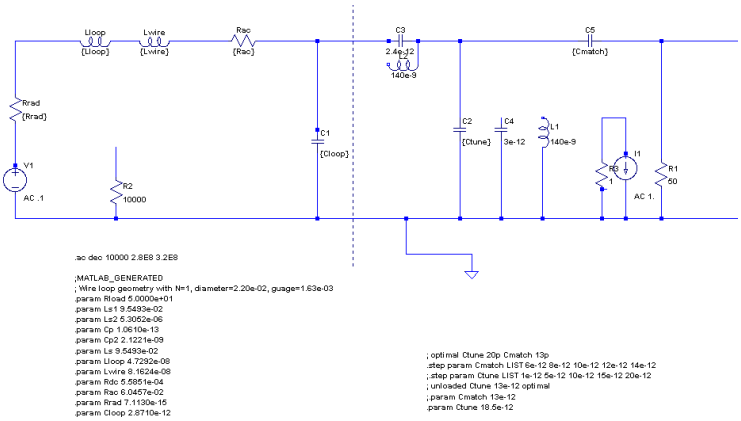

(c) SPICE implementation of the circuit model, allowing various stimuli and load conditions

Figure 5.4: Coil simulation in Spice, with geometry corresponding to Small loop (version two)

5.2.4.2 Conductor length and capacitive splits

Longer conductors will of course have greater resistance than shorter ones. Moreover, once conductor lengths reach around $\frac{\lambda_{air}}{10}$ (about 10cm for ^{1}H imaging at 7T) transmission line effects become significant; phase shifts along the wire increase, and destructive interferences decrease the peak value of the transmitted $\mathbf{B}_1$ field [Chen and Hoult, 1989]. Furthermore, dielectric losses arise as the electric field penetrates into larger sample volumes (as dictated by Maxwell's equations)[Barral, 2009]. Since the field decays rapidly with distance, a lift-off from the sample may be sufficient to mitigate these dielectric effects.

Splitting the coil with capacitors helps to reduce both the transmission line effects and the dielectric losses. However, each additional split also increase the resistive losses, due to both resistance of the solder joins and the series resistance of the capacitor itself. Splits also potentially disrupt or weaken the physical structure of the coil. For these reasons, it was determined that in this case loops would not be split, although this is area of potential improvement in later designs.

5.2.4.3 Electromagnetic Simulation

To verify the $\mathbf{B}_1$ response determined earlier and obtain an indication of off-axis response, a full-wave electromagnetic simulation may be performed. Sample output from this simulation is presented in figure 5.5; this shows the calculated intensity of the radiated field, detailed analysis of which permits determination of optimal penetration depth for a given field strength as performed in [Kumar et al., 2009], the results of which were used in determining the coil geometry.

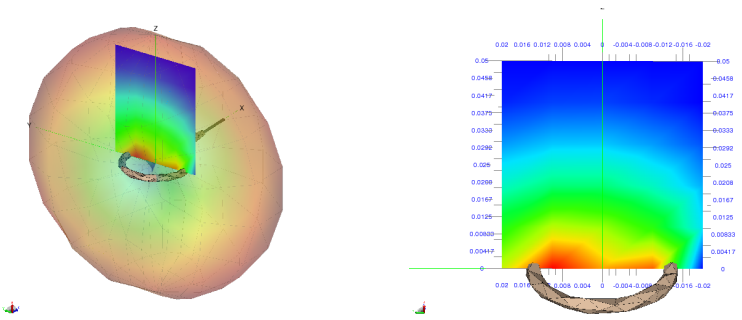

Figure 5.5: Full-wave simulation of the small loop coil showing the relative nearfield H response

5.2.5 Physical implementation

5.2.5.1 Small loop (version zero)

An initial 'proof-of-concept' coil was designed and constructed to validate the approach. Although basically functional, this unit had several shortcomings relating to component selection and geometry, and its performance was not thoroughly examined.

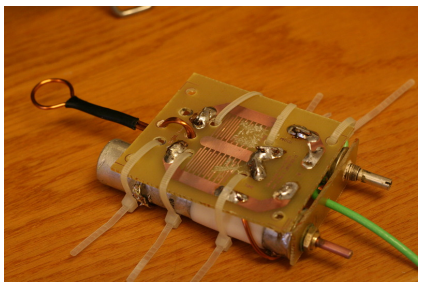

Figure 5.6: Preliminary implementation of the ^{1}Hcoil

One notable aspect of this design was the use of capacitors printed directly onto the circuit board. This promised several advantages, namely:

- reducing resistive losses through additional solder joins
- allowing easy adjustment of the capacitor value (through reducing the 'plate' area by cutting away some part of the capacitor trace)
- reducing the dependancy on specialised non-magnetic componentry

Although these capacitors performed well with regards to the above, they provided slightly lower Q and ESR than commercial offerings, were difficult to characterise accurately, and their relatively large area made them susceptable to interference and spurious interactions with nearby componentry.

5.2.5.2 Small loop (version one)

The first 'complete' design was fabricated from a modification of the original circuit board, extended to allow placement of fixed capacitors and tuning capacitors (as specified in appendix B) on-board. This layout is shown in figure 5.8.

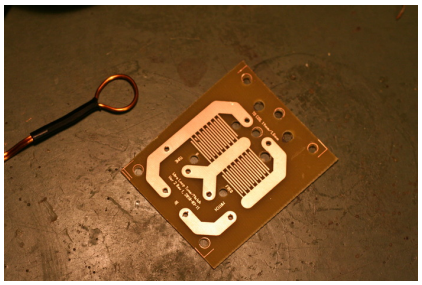

Figure 5.7: First practical implementation of the ^{1}H coil

The assembled circuit was housed in a small PVC box (100x60x25x1.5mm) for physical protection, and lined with layers of self-adhesive copper foil intended to provide additional shielding against radio frequency interference (RFI). Tune and match capacitors could be actuated by way of machined aluminium drivers, mounted on glass-reinforced-plastic rods.

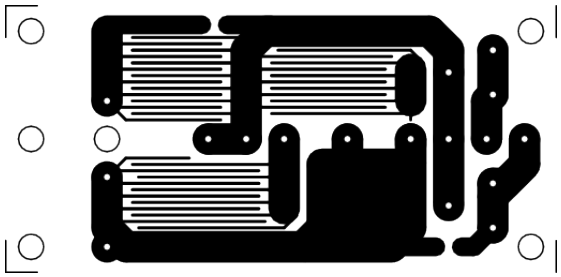

Figure 5.8: PCB layout for Small loop (version one)

5.2.5.3 Small loop (version two)

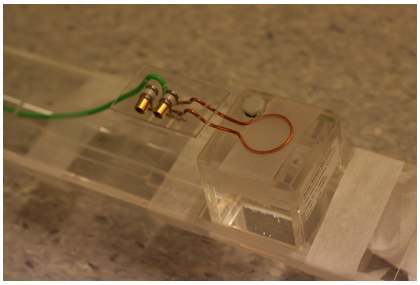

Figure 5.9: Second practical implementation of the ^{1}H coil

Initial evaluation on the above implementation showed some susceptibility to interference, presented spurious peaks in the response and somewhat poorer signal strength than expected. Furthermore, the construction was unnecessarily large given the simplicity of the circuit and somewhat impractical for mounting to objects for imaging. To address these concerns and minimise losses through superfluous solder joints and PCB traces, a second construction was completed on a 1.0mm polycarbonate sheet, with nodes formed by soldering individual component legs directly to adjacent parts. The shielded chassis was also omitted, although could of course be added retrospectively if deemed necessary. This produced a significantly more compact design, which proved more versatile in terms of mounting, albeit somewhat less robust in the absence of a fixed chassis.

5.2.6 Preliminary Tuning and Matching

An initial estimate for the series capacitor compensating for the reactance is calculated from the coil parameters substituted into the circuit model (section 5.2.2), such that the reactance approaches zero. This is automated by way of the aforementioned Matlab script, as approximately

$$\frac{1}{\omega^2 \mathrm{L}_{\mathrm{total}}} \tag{5.2.15}$$

Whilst this calculation gives a reasonable starting point, the various approximations in the model in conjunction with additional resistances and stray capacitances resulting from the physical construction and not accurately handled by the model mean that the actual value required will vary from the estimated one. Generally, a slightly lower value than calculated is used for the fixed capacitor, with variable capacitors making up the difference and allowing for various load conditions.

Chapter 6

Helmholtz Coil for In Vivo Imaging of a Fish Brain

6.1 Introduction

Further to development of the basic ^{1}H coil, an additional goal was to produce a helmholtz coil suitable for imaging the brain of a fish, potentially in-vivo. A Helmholtz coil pair consists of two identical loop coils placed symmetrically about the imaging area along a common axis, separated by a distance equal to the coil radius, with current flowing in the same direction in each coil. This provides a highly uniform field over a small volume in the middle of the two coils.

The magnetic field resulting from this arrangement is given simply by the superimposition of the responses from the individual constituent loops. It can be shown (as per [Jin, 1999], for example) that the maximum uniformity is achieved when the separation is equal to the radius of the constituent loops; from a summing of equation 4.2.1 for two loops separated by distance d, $\mathbf{B}_1$ is given by:

$$\mathbf{B}_1 = \frac{\mu_0 I a^2}{2\left[\left(\frac{d}{2}-z\right)^2+a^2\right]^{\frac{3}{2}}} + \frac{\mu_0 I a^2}{2\left[\left(\frac{d}{2}+z\right)^2+a^2\right]^{\frac{3}{2}}} \tag{6.1.1}$$

Typical response is shown in figure 6.1. It can be seen that the $\mathbf{B}_1$ field is roughly uniform for about one fifth of the distance between the loops, or equivalently a distance comparable with one fifth of the coil radius. [Haase et al., 2000, Haacke et al., 1999]

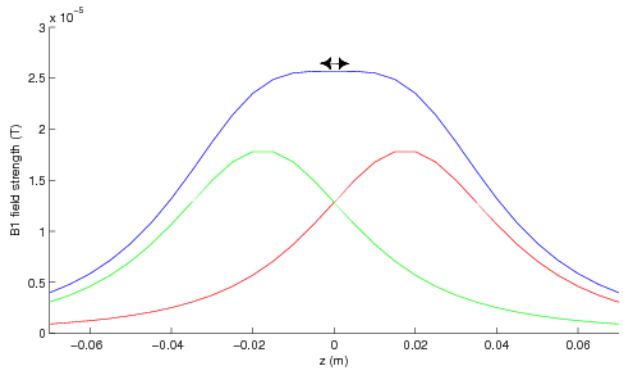

Figure 6.1: Field strength along the axis of a helmholtz coil, for r=35mm and I=1A. The lower curves show the response of the constituent loops, with the total field shown above in blue. Arrows indicate the homogenous region

6.2 Methodology

6.2.1 Basic Geometry

Construction of the Helmholtz coil is subject to rather more geometric constraints than the previously examined small loop arrangement. Firstly, it is determined that the width of the effective imaging area is roughly one-fifth of the coil radius. Secondly, the coil spacing (which is equal to the coil radius) must be sufficiently wide to allow the object of imaging to fit comfortably between the loops. These criteria give rise to a coil which is significantly larger than other designs relative to the imaging area – hence it is also more important than in previous cases to verify that there is sufficient space within the MRI hardware to accomodate the coil when mounted upon the object in the test bed.

The coil developed here is intended to fit around the head of a fish, as illustrated in figure 6.2. For effective imaging of the fish brain, an imaging area around 7mm wide is desired. This corresponds with a coil spacing of 35mm, which conveniently is adequate to accomodate a fish head. This results in loops 70mm in diameter, which for the MRI hardware in question (with 120mm available bore) allows about 40mm of free space for the tune-and-match componentry, housing, and test bed. This is close to the largest design which would be practical.

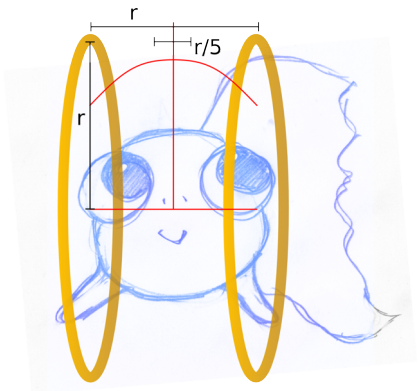

Figure 6.2: Placement of the Helmholtz coil for fish brain imaging

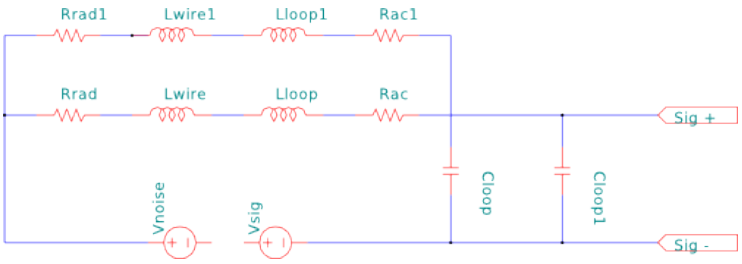

Figure 6.3: Circuit model for the Helmholtz Coil

6.2.2 Circuit Model

There are a few possible circuit configurations to implement a Helmholtz coil. One may combine the two individual loops in series, or in parallel. Alternatively, some designs have the terminals of each loop connected to form one continuous closed loop, driven by another inductively-coupled loop (perhaps located concentricly within one of the Helmholtz constituent loops).

Initial simulation showed best performance from a parallel connection of coils, with equivalent circuit model shown in figure 6.3, which is similar to the model proposed in [Murano and Kami,]. A series connection suffered from excessive AC resistance, and could not be tuned with realisable components using the previously discussed capacitative network. Furthermore, the total conductor length (in the order of 50cm) would have required several capacitive splits, adding further to the resistive losses and degrading its structural integrity.

Elements are modelled as for the single loop case, and the model is subject to the same simplifications. In addition, mutual inductance between the coil elements may affect the results.

Mutual inductance between coil elements is another factor not considered in the helmholtz model. For coils of identical radius this has an effect which may be described by

$$M_{ij} = \mu_0 r m_{ij} \tag{6.2.1}$$

where m_{ij} is a coefficient proposed in [Terman, 1943] based on the ratio of the minimum and maximum distance between coil elements ($\frac{1}{\sqrt{5}}$ for a Helmholtz coil), approximately 438.5×10^{-3} after conversion to standard units. This gives a coupling in the vicinity of 2×10^{-8} for an unloaded coil (with expectation to rise with μ).

6.2.3 Tuning and Matching

The same tune and match layout as tested on Small loop (version two) above was used for the Helmholtz coil, with component values selected based on the model presented here.

6.2.4 Physical Implementation

The physical implementation of the Helmholtz coil was similar to the Small loop (version two) in section 5.2.5.3 above; the coil itself was constructed from 1.62mm enamelled copper conductor, with tuning and matching components mounted on a polycarbonate substrate. The tune and match circuit was identical to the single loop case, with the exception that the reactance-compensating capacitor was duplicated for each side. Interconnections were made with 18swg tinned/annealed copper.

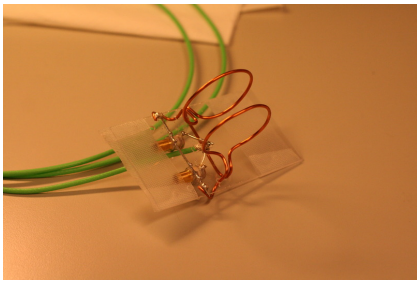

Figure 6.4: Implementation of the Helmholtz coil

The first realisation of the coil as specified could not be tuned to the desired range when loaded; in order to correct this, a reduction in loop diameter to 40mm was required. This highlights inadequacies in the model in this case, and results in a coil suitable only for imaging smaller objects than intended. Further discussion of these issues and suggested improvements appear in section 9.2.

Part III

Evaluation

Chapter 7

Procedures

In this part, the methodology used to evaluate the coils designed and implemented as described in the previous section is detailed; this is followed in subsequent chapters with with analysis of the outcomes and comparison between the various designs and commercially available systems. Various potential enhancements are also presented.

7.1 Q-factor

The Q factor (as introduced in section 2.4.3) describes the relative bandwidth of the tuned coil, that is the frequency-domain selectivity. Generally a tuned coil with higher Q is more efficient when transmitting the RF pulse, and acquires less noise (due to the narrower receive bandwidth) hence providing a superior SNR.

The Q factor can be measured from the coil's frequency response as the frequency over the full width half maximum (-3dB) bandwidth:

$$\mathrm{Q} = \frac{\omega_0}{2\Delta\omega} \tag{7.1.1}$$

This value will be somewhat dependent on the loading of the coil. Generally two values are taken to describe a typically loaded and unloaded coil ($\mathrm{Q_{loaded}}$ and $\mathrm{Q_{unloaded}}$), and the ratio of these $\mathrm{Q_{ratio}} = \frac{\mathrm{Q_{loaded}}}{\mathrm{Q_{unloaded}}}$ is computed to determine whether body noise dominates over intrinsic noise in the coil (and hence whether maximal SNR has been achieved); this is the case when $\mathrm{Q_{ratio}} > 50\%$. [Edelstein, 2006]

Previously Q was estimated in the equivalent circuit model (section 4.2.2.1); with a physical implementation Q is measured with the help of a network analyzer (see section 7.6.3). Q is first estimated in forward reflection mode, giving the response of the entire coil and tuning components.

7.2 Signal to Noise Ratio (SNR) Estimation

Signal to noise is of critical importance in image generation, as discussed in section 2.6.1. This may be estimated from the equivalent circuit as described in

section 2.6.1, and is now measured directly from images obtained in practical experiments.

There are a number of standard methods for estimating the signal-to-noise of an image; typically these are performed on images acquired of a homogeneous phantom, with surrounding air providing 'background' area within the field of view. Some of these methods are summarised in [Noureddine, 2007] as:

The AAPM method which defines a region of interest of 100 pixels, or 10% of the phantom volume. Both the signal intensity S and its standard deviation B are calculated within the region of interest. The SNR is then given simply by

$$\mathrm{SNR} = \frac{\mathrm{S}}{\mathrm{B}}$$

The first practical method is to define a region of interest covering 80% of the phantom, and calculate the mean signal value inside this region. A background region is then taken, and the standard deviation B in this area is calculated. The signal to noise ratio is then

$$\mathrm{SNR} = 0.655\frac{\mathrm{S}}{\mathrm{B}}$$

The second practical method defines a region covering 80% of the phantom as above, then four background regions of interest (ROI). The mean signal across each ROI is calculated to obtain an *offset*, and the standard deviation to get the global noise B. Then,

$$\mathrm{SNR} = \frac{\mathrm{S} - offset}{\mathrm{B}}$$

The NEMA method described in [NEMA, 2008] requires the successive acquisition of two images with identical parameters, and subtracting the two to give an image containing only noise. Taking an ROI encompassing the *imaging area* of the phantom in the subtracted image, the SNR is given from the mean signal intensity S and the standard deviation B as

$$\mathrm{SNR} = \sqrt{2}\frac{\mathrm{S}}{\mathrm{B}}$$

The NEMA method is considered one of the more robust methods for SNR estimation, as the alternative methods proposed do not take into account offset (or consider this only coarsely).

Moreover, as this work deals with surface coils which by design are have broadly inhomogeneous response, the NEMA method proves most suitable for rejecting these immutable effects. Indeed the NEMA method is explicitly proposed for application to surface coils where field inhomogeneity is expected. To this end, analysis hereafter is performed with the NEMA method, applied to a (somewhat arbitrarily defined) elliptical region with long axis of half the phantom diameter and short axis one half of this, centered about the peak response in the imaging area as shown in figure 7.1a.

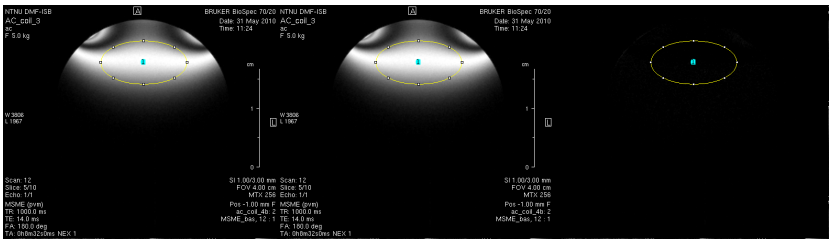

(a) First acquisition **(b)** Second acquisition **(c)** Difference

Figure 7.1: Images used in the NEMA method for SNR estimation

7.3 Usable Area/B_1 Homogeneity

The homogeneity of the $\mathbf{B}_1$ field generated by a coil will determine the uniformity of intensity in the resulting image, as well as setting constraints on the volume over which the coil may be used effectively. [1]

$\mathbf{B}_1$ homogeneity of the real coil is assessed through multiple acquisitions at different flip angles. Quantitative analysis may be obtained through performing numerical analysis on the amplitude curve over a large number of acquisitions, although this is only accurate when dielectrical resonances can be suppressed, for example when working with a silicone oil phantom.

For more approximate numeric results, a gradient echo sequence with a short angle (say around 30 degrees) and long relaxation time may be used, which generates a map of the received intensity. Generally this features a black region very near the winding due to saturation, and otherwise a fading intensity as distance increases. For a homogeneous phantom, this intensity may be used to calculate correction factors for intensity throughout the image.

A more simple qualitative visual representation of homogeneity may also be obtained, by acquiring an image with a very high flip angle.Taking a spin echo image with a nominal flip angle of multiple full rotations (for example, 720°), a series of bands become visible. Since the actual flip angle observed will be proportional to the signal strength, dark bands appear in areas where little signal was available for refocussing – corresponding to an effective flip angle around a multiple of 180°in that area. Similarly, bright bands correspond with effective flip angles equivalent to 90°pulses, that is $90 + (n\cdot)°$ [Crozier et al., 1995]. For the purposes of this analysis, the latter method of $\mathbf{B}_1$ visualisation will be used.

7.4 Image Intensity Uniformity

A quantitative measure of uniformity is largely meaningless in the context of surface coils, since these by definition are only effective over a small volume near the coil, and tend to have a generally non-uniform response even within the effective volume. Nonetheless, a rough indication of uniformity over the

[1] General information in this section was graciously provided through email correspondence with Prof Michael Horn (Göteburg University) and Sascha Köhler (Bruker Biospin).

effective imaging area may be obtained in a similar way as for a more uniform system. A ROI is selected covering a large proportion of the effective imaging area (the same ROI as used in the SNR calculations above is chosen). Then, the minimum and maximum values of the signal intensity inside this area are identified, and uniformity is estimated by:

$$\text{uniformity} = \left(1 - \frac{max - min}{max + min}\right) \times 100 \tag{7.4.1}$$

A figure around 80% is considered reasonable for volume coils, although much lower figures are expected for surface coils.

7.5 Artifacts

There are a very wide variety of artifacts which may arise in MR imagery as described in section 2.6.3, which are influenced by a number of parameters including the object to be imaged, the imaging coil, the other imaging hardware, and properties of the scan sequence being performed. The interactions between these components are complex, hence it is often difficult to attribute a visible artifact to one specific component. The variety of artifacts also makes general quantitative assessment difficult.

A close visual inspection of acquired images is performed to locate artifacts known to be often attributable to coil or RF hardware. Additionally, a rough numeric calculation may be performed to estimate the percentage of ghosting in acquired images. Five ROIs are defined, one inside the phantom and the others in the background, covering the middle part of each edge (forming points of a cross shape). The percentage of ghosting is then given by:

$$\%\text{ghosting} = \frac{|S_{top} + S_{bottom} - (S_{left} + S_{right})|}{2S_{center}} \tag{7.5.1}$$

Ghosting of less than 3% is considered minimal according to American College of Radiology (ACR) recommendations.[Noureddine, 2007]

7.6 Evaluation Configuration

7.6.1 Test Subjects

Four coils were considered in the assessment:

Small loop (version one) consisted of a 20mm loop mounted on a FR4 substrate, with copper-etched tune and match circuitry. See section 5.2.5.2

Small loop (version two) consisted of a 20mm loop with tune-and-match components directly soldered, minimising resistive losses. See section 5.2.5.3

Helmholtz coil consisted of a 50mm Helmholtz pair, with tune-and-match components soldered directly. This coil is detailed in chapter 6.1

Bruker 300-75 is a commercial surface coil (Bruker 300-75 Mini SUC20 1P T6614), operating on ^{31}P (75MHz) and ^{1}H (300MHz). Only the ^{1}H channel was used.

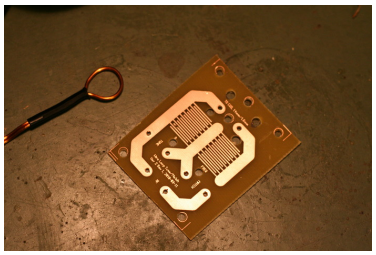

(a) Small loop (version one)

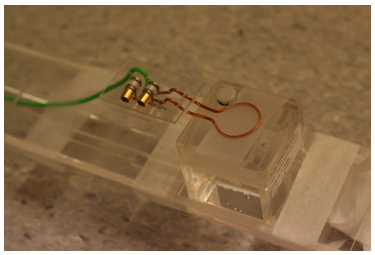

(b) Small loop (version two)

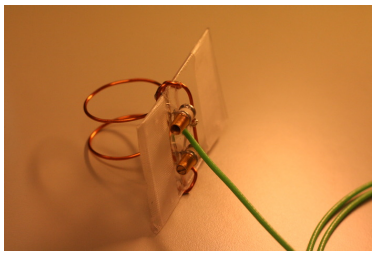

(c) Helmholtz coil

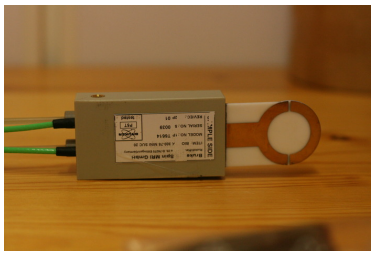

(d) Bruker 300-75

Figure 7.2: Surface coils for evaluation

7.6.2 Test objects

Phantom one was a small glass sphere, approximately 25mm diameter, containing 3mmol $CuSO_4$ solution. This was intended to provide a homogeneous object to assess the spatial variation of the response.

The head of a dead fish was used to provide a realistic imaging scenario, in terms of loading, chemical composition, tissue inhomogeneities, contrast and spatial resolution. The head was provided by a small cod.

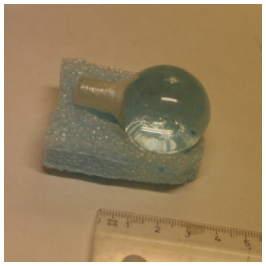

(a) Phantom one

(b) Fish head

Figure 7.3: Phantoms used for testing

7.6.3 Test Hardware

A Bruker Biospec Avance 70/20AS small animal scanner[2], configured as detailed below, was used for all imaging experiments:

Magnet	Magnex Scientific 7T210AS, 200mm bore
Gradient	BGA12, water-cooled, 400mT/m, 120mm bore
Shim	B-S20
Preamp	HPR/2 2x500W

The operating principles of the MRI scanner are detailed in the introduction, section 2.2.5. The user interface to this scanner was through the standard Bruker Paravision software suite.

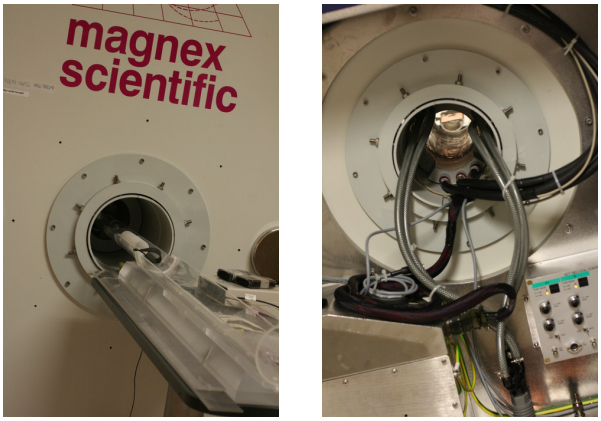

(a) Front **(b)** Rear

Figure 7.4: Bruker 7T Small Animal Scanner

A Hewlett Packard HP8753E network analyzer[3] was used for all preliminary out-of-magnet tuning and evaluation, plus for Q factor estimation.

The network analyzer has various modes of operation, but in broad terms it transmits a sweep of stimulus frequencies into the circuit to be tested, and measures the response of the circuit as a function of frequency. A typical analyzer may have two ports, each of which can be used to send a stimulus and/or listen for a response. The measured response may be a reflection of the stimulus back to the same port due to changing impedance conditions encountered as it travels through the circuit. This mode of operation is referred to as 'S11' or forward reflection mode, where 'S' donates the reflection coefficient (see equation 4.3.1), the first '1' identifies the device port used to send the stimulus and the second '1' identifies the device port used to listen for a response. Another mode of operation is forward transmission mode (denoted 'S12'), where a secondary 'sniffer' coil is placed within the field of the first coil, attached to the second port of the analyzer and used to listen for a response. This second mode

[2] situated in MILab's MR-senteret
[3] on loan from Gruppe for radioteknikk, Institutt for elektronikk og telekommunikasjon, NTNU

may be used to measure the relative field strength, and can give more accurate Q factor measurements.

Various display formats are available; two are of particular interest for this application. The first is log-magnitude mode, which displays the magnitude response as a function of frequency. This is used for tuning the coil to the desired frequency, and measuring the magnitude and Q factor of the resonant peak (minima and span-tracking functions on the analyser assist in automating these measurements).

The other relevant mode provides a smith chart display (discussed in [Bowick, 1997]). Here it is possible to visualise the impedance and phase response of the coil as a function of frequency; this is useful for matching the network to the desired impedance at the target frequency.

The device used offers various additional interfaces (including an RS/232 port and a floppy drive) to allow capture and transfer of measurement data and graphics to a computer for further analysis or reporting.

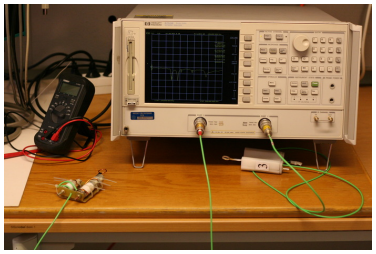

(a) HP8753E Network Analyzer

(b) Sniffer Coil for forward transmission mode

Figure 7.5: Network Analyzer for out-of-magnet measurements

7.7 Practical procedure

7.7.1 Preparation

Prior to evaluation, coils were initially tested against a phantom as defined in 7.6.2. This was placed upon and secured to a test bed, with the coil mounted over the top of the phantom, in contact with it. As necessary for effective imaging, the coil alignment is such that the $\mathbf{B}_1$ field is normal to $\mathbf{B}_0$ when loaded in the machine. For practicality, tuning and matching to the phantom-loaded coil was performed outside the bore, using the machine's wobble function. The phantom with coil mounted was then inserted into the bore and aligned to the isocenter, and correct tuning verified.

7.7.2 Measurements in the magnet

- Initially, an `A_TRIPLOT_GE_bas` sequence was performed to calibrate initial gains and pulse parameters and acquire orthogonal image slices for adjusting the scan geometry to suit the object placement.

- A rough spin-echo acquisition was made to verify the calibration and geometry obtained above, allowing for further manual adjustment if necesary.
- A series of spin-echo acquisitions (see 2.3.1) were made; two TE/TR variations were taken offering different weighting and signal strength, and each variation was performed twice to facilitate SNR calculation by the NEMA method.

Parameter	Test One	Test Two
Procedure	`MSME_bas`	
TE	14ms	10.7ms
TR	1000ms	250ms
Nrep	2	
Nav	1	
Nslices	10	
Slice thickness	1mm	
Slice spacing	3mm	
Field of View	40mmx40mm	
Matrix size	256x256	

- Similarly, a series of gradient-echo acquisitions (section 2.3.3) were taken; as above, each variation was performed twice to allow for SNR calculation. The long TR is suitable for rough numerical $\mathbf{B}_1$ field mapping.

Parameter	Test One	Test Two
Procedure	`MGE_bas`	
TE	4ms	5.4ms
TR	1500ms	250ms
Nechos	1	
Flip angle	40^o	
Nslices	10	
Slice thickness	1mm	
Slice spacing	3mm	
Field of View	40mmx40mm	
Matrix size	256x256	
Repetitions (manual)	2	

- Finally, a high flip angle spin echo scan was made, with a nominal flip angle of 720°. This was achieved by manually adjusting the magnitude and duration of the calculated excitation pulse, whilst leaving the refocussing pulse unchanged.

7.7.3 Measurements on the Network Analyzer

Having been tuned and matched to *Phantom one* for use in the magnet, each coil was subsequently attached to the network analyzer (see 7.6.3). Measurements were taken of the tuned peak in S11 mode for the loaded and unloaded coil.

- The general form of response over a broad range of frequencies was validated by looking at the log magnitude response from 0 to 1GHz.
- A finer analysis was performed in a narrower band surrounding the nominal peak, generally in the 280-320MHz range. A reference cursor was set to track to the minimal response (corresponding to the resonant peak), and 3dB delta points around this point minimum were used to calculate the Q factor. In all cases it proved necessary to use a time-averaging window of 30 samples to provide a sufficiently stable measurement (see discussion in **??**).
- Matching was verified by inspection in smith chart mode.

At any stage, graphical and raw data may be exported from the device for reporting and additional analysis.

7.7.4 Post-processing and Analysis of the Acquired Images

7.7.4.1 Software Requirements

As well as the standard Bruker Paravision suite, several additional software packages were utilised to assist in handling and evaluation of the captured images. These include:

- `pvconv.pl` for batch conversion of ParaVision data into the more widely supported Analyze format.
- `fsl` for visualizing the converted data
- `medcon` for batch extraction of image slices into individual raster images
- `ImageJ` for stack visualisation, region-of-interest definition and analysis and image arithmetic.
- `gnumeric` spreadsheet for calculations based on ROI data obtained with ImageJ

7.7.4.2 Analysis procedure

Data were extracted from the ParaVision repository using `pvconv.pl` and `medcon` programs. Relevant slices were then loaded into ImageJ, where regions of interest were defined according to the procedures specified in section **??**. Difference images for NEMA-method SNR calculation were obtained using the builtin 'Image Calculator' function to subtract the source images in 32-bit (signed float) mode. Basic statistics were measured directly in ImageJ (in batch for every ROI) and imported into a `gnumeric` spreadsheet where the analytic formulae were implemented. The effective imaging depth is measured as the depth at which the received signal intensity is attenuated by 3dB (in the case of the Helmholtz coil, this is measured across the central peak).

Chapter 8

Results

8.1 Coil Response and Quality Factor

Initial measurements for the coil frequency response and estimates of the quality factor, by methods described in section **??**, are given in table 8.1. Corresponding plots of the raw data from the network analyzer are presented in appendix A.

		Loaded		Unloaded		
Coil	Method	Q	S	Q	S	$Q_{ratio}\%$
Small loop (version one)	direct	700	35	2000	42	35
Small loop (version two)	direct	400	36	2110	55	19
Helmholtz coil	direct	300	13	1200	36	25
Bruker 300-75	direct	900	22	5000	40	18

Table 8.1: Coil response and quality factor, measured with the network analyzer

8.2 Signal Quality as Measured on the Scanner

Measures of various aspects of image quality, evaluated by the methods described in section 7.7 follow in table 8.2; raw images are contained on the CD accompanying this report. In the results table, SNR, Uniformity and Ghosting represent results of the equations presented in chapter 7, with SNR being determined by the NEMA method. The depth column indicates the measured distance along the imaging band, before the signal strength drops by 3dB. The best and worst performing coil in each aspect are highlighted in green and red respectively. The Helmholtz coil is also investigated specifically in the theoretically-determined uniform area, highlighting its advantage in this respect.

Coil	Sequence	TE (ms)	TR (ms)	SNR %	Uniformity %	Ghosting %	Depth (mm)	B_1 Field Map
Small loop (version one)	SE	14	1000	99	45	0.009	8.2	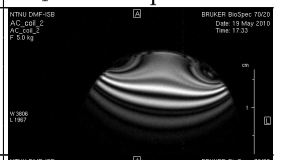
	SE	10	250	52	40	0.186	8.5	
	GE	4	1500	80	37	0.000	7.3	
	GE	5.4	250	67	50	0.036	8.5	
				75	43	0.058	8.1	
Small loop (version two)	SE	14	1000	93	58	0.026	10.6	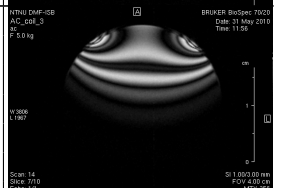
	SE	10	250	38	50	1.062	10.6	
	GE	4	1500	76	38	0.000	7.3	
	GE	5.4	250	67	47	0.011	7.9	
				69	48	0.274	9.1	
slightly detuned	SE	14	1000	36	27		7.3	
more detuned	SE	14	1000	13	6		5.4	
Bruker 300-75	SE	14	1000	116	22	0.004	11.5	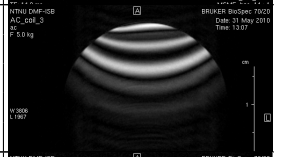
	SE	10	250	53	19	0.162	11.5	
	GE	4	1500	100	43	0.001	6.7	
	GE	5.4	250	83	44	0.004	7.9	
				88	32	0.043	9.4	
Helmholtz coil	SE	14	1000	54	52	0.085	9.1	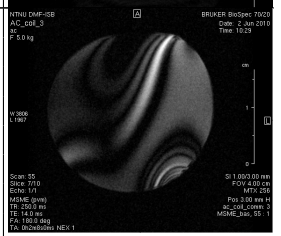
	SE	10	250	26	44	0.430	8.8	
	GE	4	1500	36	21	0.058	9.1	
	GE	5.4	250	27	22	0.273	12.1	
				36	35	0.212	9.8	
uniform region	SE	14	1000	56	78		4	
	SE	10	250	29	69		4	
				43	73		4	

Table 8.2: Summary of Image Quality Measurements; details in the corresponding text section 8.2

8.3 Imaging Artifacts

No coil-attributed artifacts were visible for Small loop (version one), Helmholtz coil and Bruker 300-75. However, Small loop (version two)showed a faint zipper artifact and a 'spot' of noise, both of which may be attributed to RF interference. These are shown in figure 8.1.

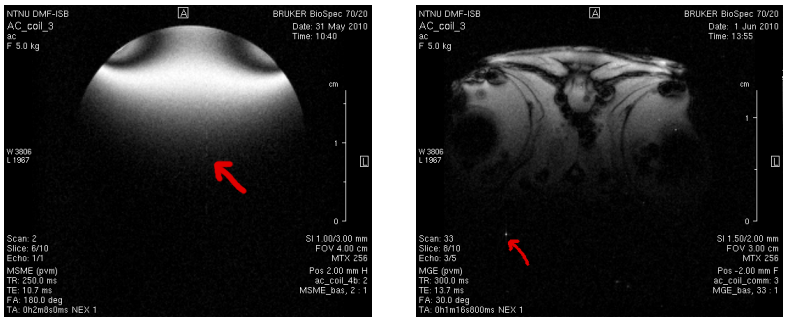

Figure 8.1: Artifacts observed when imaging with Small loop (version two)

8.4 Image Acquisition

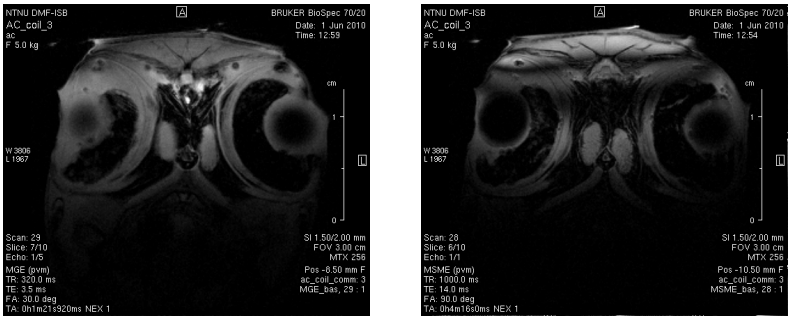

(a) Bruker 300-75

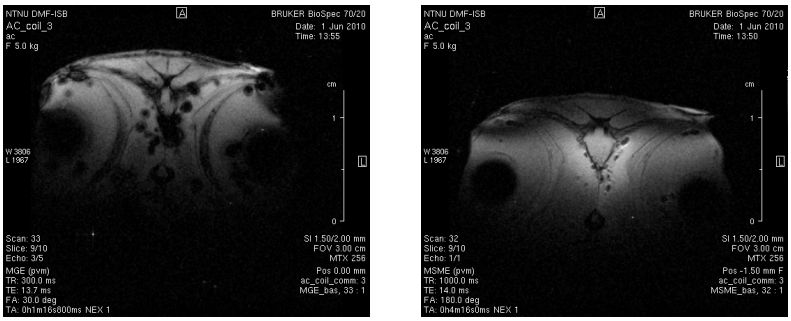

(b) Small loop (version two)

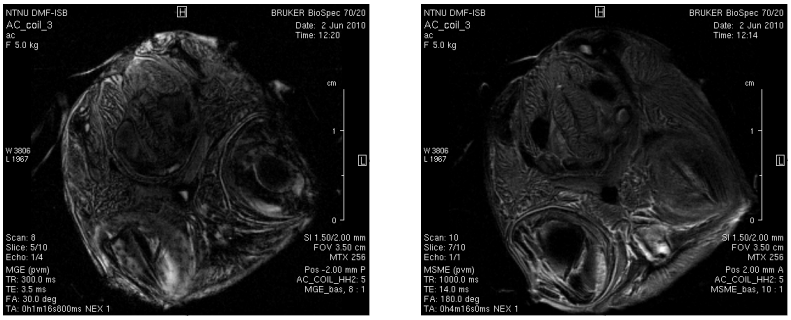

(c) Helmholtz coil

Figure 8.2: Imaging Performance; the left-hand column shows results for a gradient-echo sequence, the right-hand column shows output for a spin-echo sequence. Sequence parameters (TE, TR) are the same for each coil.

Chapter 9

Discussion

9.1 Coil Response and Quality Factor

The coil response measurements obtained in section 8.1 show acceptable Q values from the tuned coils in S11 mode, albeit somewhat lower than for the benchmark Bruker 300-75 device. A $Q_{\mathrm{ratio}} < 50\%$ in all cases indicates body noise dominance, a condition requisite for optimal SNR. The measured reflection coefficient at the resonant peak is again somewhat inferior to the Bruker 300-75, although in a similar order.

9.2 Tuning and Matching

For the small loop coils the tuning and matching circuit was found to perform adequately, albeit with some issues relating to the stability of the tuning – this was excessively dependent on orientation of the cable and placement of the sample. Nonetheless, with patience the coil could be tuned suitably for of the available loads.

The Helmholtz coil proved somewhat less effective in this regard; the initial implementation at the target scale could not be tuned to the required band using the tune-and-match circuit as implemented; it was necessary to scale down the coil size, resulting in a reduction in the effective imaging area and placing undesirable constraints on the physical size of objects around which the coil could be placed. Even with the smaller implementation, the tuning was excessively dependent on loading conditions, perhaps attributable to inductive coupling through the sample (not considered by the circuit model) or asymmetrical loading between the two sides of the coil.

9.3 Image Quality

In terms of image acquisition all designs performed adequately, in the sense that they could be tuned and matched appropriately for the ^{1}H imaging of the various test objects and returned acceptable signal levels for image generation. As expected a strong correlation is seen between the measured Q and reflection

coefficient (section 8.1) and the measured SNR, with the relative performance of each coil being equivalent in each case.

SNR of the produced coils is slightly inferior to the benchmark Bruker 300-75, but still adequate for practical application. Measured uniformity is very good, superior to the benchmark.

9.4 Imaging Area

The effective imaging area for each coil agreed with the target design values.

For the single loop surface coils, a very strong (saturating) response is seen in the immediate vicinity of the wire, with a smoother bands at a moderate distance. The observed field pattern was quite regular and matched expectations, with slight variations due to irregularities in the construction.

The field from the Helmholtz coil was rather less regular than anticipated, and hence the optimal imaging position difficult to determine. It was noted that the tuning of this coil was very heavily dependent on the load conditions. Given this dependency, it is likely that any asymmetry in the loading between the two parallel-wired loops resulted in different resonant conditions on each side, hence producing a very irregular field as observed. This could potentially be resolved with a series connection of the constituent coils.

9.5 Imaging Artifacts

All coils performed very well in terms of visible and measurable artifacts, with measured ghosting well below 1% in almost all acquisitions. Performance of Small loop (version two) was slightly poorer than the other coils, and this was the only device presenting clearly visible artifacts, in the form of a slight zipper artifact likely resulting from interference in the absence of shielding around the tune and match circuitry.

9.6 Practical Considerations

Although the primary focus of assessment in this report is on quantifiable parameters in the image, there are a number of other considerations in determining the usefulness of the designs to practical applications – particularly in terms of usability, robustness and flexibility of positioning.

9.6.1 Tuning and Matching controls

The implementations evaluated here employed small trimmer capacitors requiring an external tool for adjustment; this means that tuning and matching must generally be performed outside of the magnet. Although for designs with more stable tuning this is acceptable, there was an observed tendency for the slightly different loading conditions when the assembly was placed inside the magnet to offset the resonant peak slightly, often requiring some correction. Repeated adjustment requiring removal of the device from the magnet at each stage proved rather tedious and is far from desirable in routine usage. This of

course could be alleviated by substituting larger tuning capacitors of compatible specification but featuring a shaft for adjustment (such as the Voltronics or Sprague-Goodman components listed in section B), bearing in mind that these will occupy substantially more space, require more elaborate housing and come at a significantly higher cost.

9.6.2 Housing

Coils were initially designed for mounting in a small PVC box for physical support, lined with layered copper foil for electromagnetic shielding. This arrangement proved somewhat cumbersome and limited the options for mounting of the coil to the object; the shielding also had no observable effect (presumably since the MR hardware itself provided adequate shielding in this instance). Operating without the housing provided good flexibility, but is not a robust long-term solution; preferably a more compact, better suited housing should be implemented.

9.6.3 Affects of Loading and Cable Orientation

The frequency response of each implementation proved somewhat dependent on the loading (as one would expect), but also highly dependent upon the cable orientation. This made tuning and matching somewhat problematic, particularly given the difficulties in actuating the tuning controls when the device was mounted in the magnet, as discussed above. This is likely a result of the high Q design and poor impedance matching away from the resonant peak.

Chapter 10

Further work

As detailed in the previous chapter, the most significant shortcoming of the simple loop designs implemented here is stability of the response, with respect to movements of the coil or cable. It is suggested that an alternative to the two-element capacitive matching network may offer improvements in this area. Specifically, it is suggested that a three-element T network with capacitive and inductive components be employed, as proposed in section 5.2.3. This design is likely to provide additional gains in terms of Q factor flexibility, with only slight drawbacks in terms of complexity and additional resistive losses.

Additionally, the option of a capacitive split in the loop conductor should be evaluated in further detail; this may assist in suppression of losses through transmission line effects, particularly in the longer conductor of the Helmholtz loop, thereby offering a stronger signal. Effective design for a split loop would require modification to the circuit model used here, and the additional capacitive reactance may require an alternative design for the tune-and-match circuitry.

Asymmetrical loading of the loops in the Helmholtz structure has been identified as a possible cause of the very irregular field pattern observed, and may be mitigated to some degree by serial wiring of these parts.

Finally, further consideration should be given to the enclosure in order to provide adequate physical protection, shielding from RFI and more convenient actuation of the tune and match controls.

Chapter 11

Conclusions

Per the objectives of this project, a series of functional transmit/receive coils suitable for imaging in a 7T animal scanner were successfully developed and evaluated. The approach proved versatile to a number of designs, and the product very economical when compared with commercial equivalents. Although the signal quality was slightly inferior to that of the reference unit, the performance is considered adequate for many imaging applications.

The development processes employed here have proven effective, and could be directly applied for future designs. Several opportunities exist for refining the actual design into a product suitable for routine use, and a number of such enhancements have been proposed in this report. These address all the identified issues, and it is anticipated that implementation of the recommendations would result in a product with comparable performance to the benchmark unit, and advantages in terms of cost and specific customisation to the particular application.

Part IV

Appendices

Appendix A

Raw Results

A.1 Overview

In this section, raw results from coil measurements on the network analyzer are presented.

A.2 Small loop (version one)

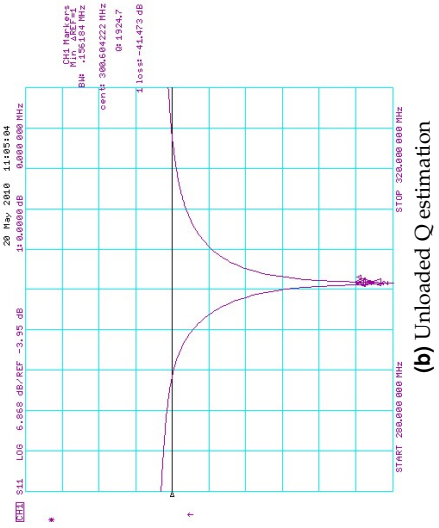

(a) Frequency Response

(b) Unloaded Q estimation

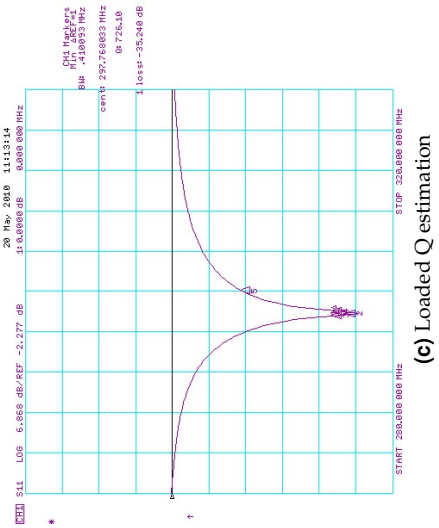

(c) Loaded Q estimation

A.3 Small loop (version two)

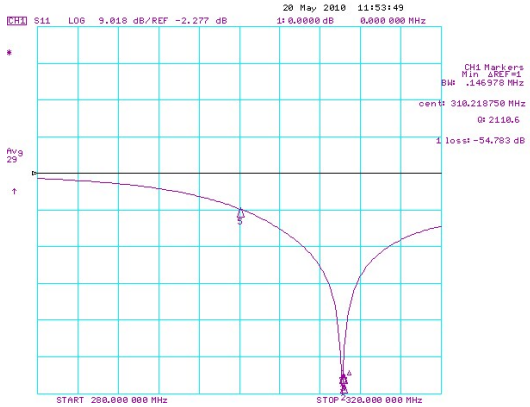

(d) Unloaded Q estimation

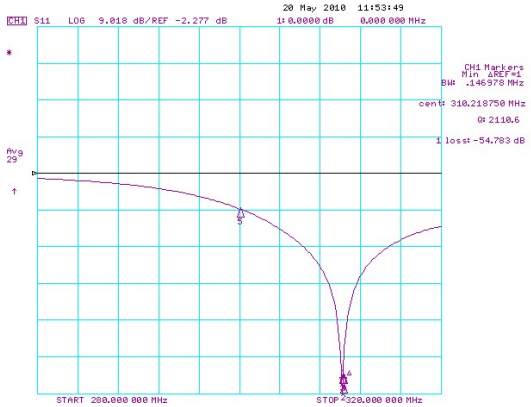

(e) Loaded Q estimation

A.4 Helmholtz coil

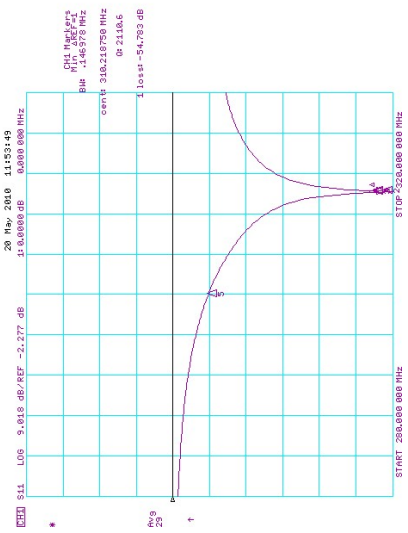

(f) Unloaded Q estimation

(g) Loaded Q estimation

A.5 Bruker 300-75

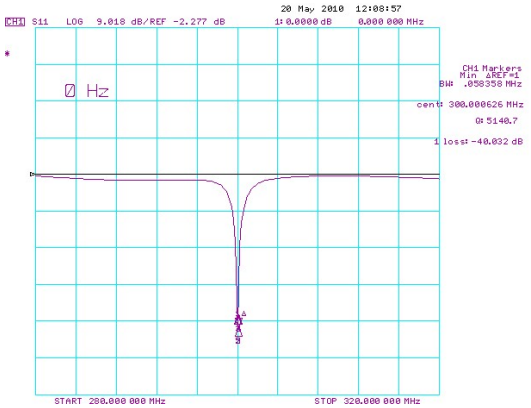

(h) Unloaded Q estimation

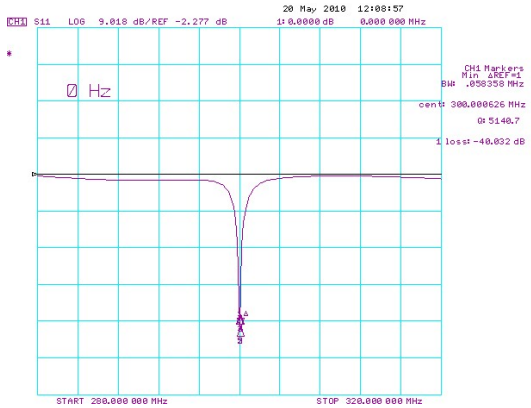

(i) Loaded Q estimation

Appendix B

Components

Wire and Interconnects	
	18SWG tinned/annealed copper
	16SWG enameled copper
Tuning Components	
Temex Ceramics	501 CHB series non-magnetic capacitors
Temex Ceramics	AT55H01 trimmer capacitors
Guangdong Yiye	25pF non-magnetic air trimmer
Suggested Alternatives	
Voltronics	VOLNMNT706E
SGNM	SGNM1209

Bibliography

[wol, 2010] (2010). Wolfram | Alpha knowledgebase. http://www.wolframalpha.com/.

[Barral, 2009] Barral, J. (2009). building rf surface coils for MRI.

[Bloch et al., 1946] Bloch, F., Hansen, W., and Packard, M. (1946). Nuclear induction. *Physical review*, 70(7-8):460–474.

[Bosshart, 1983] Bosshart, W. (1983). *Printed circuit boards: design and technology*. Tata McGraw-Hill.

[Bowick, 1997] Bowick, C. (1997). *RF circuit design*. Newnes.

[Burian and Hajek, 2004] Burian, M. and Hajek, M. (2004). Linear microstrip surface coil for MR imaging of the rat spinal cord at 4.7 T. *Magnetic Resonance Materials in Physics, Biology and Medicine*, 17(3):359–362.

[Chen and Hoult, 1989] Chen, C. and Hoult, D. (1989). *Biomedical magnetic resonance technology*. Adam Hilger Bristol.

[Collins, 2006] Collins, C. (2006). Radiofrequency Field Calculations for High Filed MRI. *Ultra High Field Magnetic Resonance Imaging*.

[Crozier et al., 1995] Crozier, S., Luescher, K., Forbes, L., and Doddrell, D. (1995). Optimized small-bore, high-pass resonator designs. *Journal of Magnetic Resonance, Series B*, 109(1):1–11.

[Doty et al., 2007] Doty, F., Entzminger, G., Kulkarni, J., Pamarthy, K., and Staab, J. (2007). Radio frequency coil technology for small-animal MRI. *NMR in Biomedicine*, 20(3):304–325.

[Edelstein, 2006] Edelstein, W. A. (2006). Principles and Modeling of Radiofrequency Coil Signal Detection and Image Production.

[Gregory, 1997] Gregory, C. (1997). Mri artifact gallery. http://chickscope.beckman.uiuc.edu/roosts/carl/artifacts.html.

[Guendouz et al., 2008] Guendouz, L., Ghaly, S., Hedjiedj, A., Escanyé, J., and Canet, D. (2008). Improved Helmholtz-type magnetic resonance imaging coils with high-B1 homogeneity-Spherical and ellipsoidal four-coil systems. *Concepts in Magnetic Resonance Part B: Magnetic Resonance Engineering*, 33(1):9–20.

[Haacke et al., 1999] Haacke, E., Thompson, M., and Brown, R. (1999). *Magnetic resonance imaging: physical principles and sequence design*. Wiley New York.

[Haase et al., 2000] Haase, A., Odoj, F., Von Kienlin, M., Warnking, J., Fidler, F., Weisser, A., Nittka, M., Rommel, E., Lanz, T., Kalusche, B., et al. (2000). NMR probeheads for in vivo applications. *Concepts in Magnetic Resonance Part A*, 12(6):361–388.

[Hoult and Richards, 1976] Hoult, D. and Richards, R. (1976). The signal-to-noise ratio of the nuclear magnetic resonance experiment. *Journal of Magnetic Resonance (1969)*, 24(1):71–85.

[Jin, 1999] Jin, J. (1999). *Electromagnetic analysis and design in magnetic resonance imaging*. CRC.

[Kaye and Laby, 1995] Kaye, G. and Laby, T. (1995). Tables of physical and chemical constants 16th edn (Harlow).

[Kelley, 2006] Kelley, D. (2006). Hardware Considerations in Ultra High Field MRI. *Ultra High Field Magnetic Resonance Imaging*, pages 45–57.

[Kumar and Bottomley, 2008] Kumar, A. and Bottomley, P. (2008). Optimized quadrature surface coil designs. *Magnetic Resonance Materials in Physics, Biology and Medicine*, 21(1):41–52.

[Kumar et al., 2009] Kumar, A., Edelstein, W., and Bottomley, P. (2009). Noise figure limits for circular loop MR coils. *Magnetic resonance in medicine: official journal of the Society of Magnetic Resonance in Medicine/Society of Magnetic Resonance in Medicine*.

[Kuperman and Kuperman, 2000] Kuperman, V. and Kuperman, V. (2000). *Magnetic resonance imaging: physical principles and applications*. Academic Pr.

[Loudet, 2009] Loudet, L. (2009). SID Monitoring Station – Magnetic Loop Antenna Theory. http://sidstation.lionelloudet.homedns.org/antenna-theory-en.xhtml.

[MacLaughlin, 1989] MacLaughlin, D. (1989). Coaxial cable attenuation in NMR sample coil circuits. *Review of Scientific Instruments*, 60:3242.

[Maxwell, 1865] Maxwell, J. (1865). A dynamical theory of the electromagnetic field. *Philosophical Transactions of the Royal Society of London*, 155:459–512.

[Mispelter et al., 2006] Mispelter, J., Lupu, M., and Briguet, A. (2006). *NMR probeheads for biophysical and biomedical experiments: theoretical principles & practical guidelines*. Imperial College Pr.

[Murano and Kami,] Murano, K. and Kami, Y. Low Frequency Radiated Immunity Test Using Three-Dimensional Helmholtz-Coil Set (Special Issue on Recent Progress in Electromagnetic Compatibility Technology).

[NEMA, 2008] NEMA (2008). NEMA Standards Publication MS 1-2008: Determination of Signal-to-Noise Ratio (SNR) in Diagnostic Magnetic Resonance Imaging.

[Neumaier et al., 2009] Neumaier, M., Niessen, H., Kaulisch, T., and Stiller, D. (2009). Inductively coupled helmholtz coil on a dedicated imaging platform for the in vivo 1H-MRS measurement of intramyocellular lipids in the hind leg of rats. *Magnetic Resonance in Medicine*, 62(4):1036–1041.

[Noureddine, 2007] Noureddine, Y. (2007). Improvement of a quality assurance program for a 7 Tesla small animal MR-scanner. NTNU Institutt for Sirkulasjon og Bildediagnostikk.

[Redpath, 1998] Redpath, T. (1998). Signal-to-noise ratio in MRI. *British Journal of Radiology*, 71(847):704.

[Robitaille, Pierre-Marie and Berliner, Lawrence, 2006] Robitaille, Pierre-Marie and Berliner, Lawrence (2006). *Ultra High Field Magnetic Resonance Imaging*. Springer.

[Rodríguez et al., 2009] Rodríguez, A., Hernández, R., Salgado, P., and Barrios, F. (2009). Concentric dual-loop rf coil for magnetic resonance imaging. *Revista Mexicana de Física*, 49(002).

[Sadiku, 2001] Sadiku, M. (2001). *Elements of electromagnetics*. Oxford university press New York.

[Sahara et al.,] Sahara, T., Tsutsui, H., Hashimoto, S., Mochizuki, S., Yamasaki, K., Kondo, H., Miyazaki, T., Motozuka, M., Okuyama, K., Osaka, J., et al. Wireless Radio Frequency Coil for Magnetic Resonance Image of Knee Joint. *image*, 6:10.

[Suits et al., 1998] Suits, B., Garroway, A., and Miller, J. (1998). Surface and Gradiometer Coils near a Conducting Body: The Lift-off Effect* 1. *Journal of magnetic Resonance*, 135(2):373–379.

[Terman, 1943] Terman, F. (1943). *Radio engineers' handbook*. McGraw-Hill New York.

[Vaughan et al., 2002] Vaughan, J., Adriany, G., Garwood, M., Yacoub, E., Duong, T., DelaBarre, L., Andersen, P., and Ugurbil, K. (2002). Detunable transverse electromagnetic (TEM) volume coil for high-field NMR. *Magnetic Resonance in Medicine*, 47(5):990–1000.

[Viohl and Gullberg, 2005] Viohl, I. and Gullberg, G. (2005). Tuning and matching networks for MR imaging and spectroscopy. *Journal of Magnetic Resonance Imaging*, 4(4):627–630.

[Webb, 1988] Webb, S. (1988). *The physics of medical imaging*. Taylor & Francis.

[Westbrook et al., 2005] Westbrook, C., Roth, C., and Talbot, J. (2005). *MRI in Practice*. Wiley-Blackwell.

[Zelaya et al., 1997] Zelaya, F., Roffmann, W., Crozier, S., Teed, S., Gross, D., and Doddrell, D. (1997). Direct visualisation of B1 inhomogeneity by flip angle dependency. *Magnetic resonance imaging*, 15(4):497–504.